Composite Structures 372 (2025) 119511

Contents lists available at ScienceDirect

Composite Structures

journal homepage: www.elsevier.com/locate/compstruct

Automated composite design generation and optimization using variable angle tow plies for aerospace applications☆

Pezhman Pourabdollah [a,b,*], Lennart Finger [b], Rachid Alhourani [b], Tim Frerich [b], Raphael Höfer [a,b], Felix Gehlhoff [a], Benedikt Kriegesmann [c]

[a] Helmut Schmidt University Hamburg, Holstenhofweg 85, 22043 Hamburg, Germany
[b] CTC GmbH (An Airbus Company), Airbus-Straße 1, 21684 Stade, Germany
[c] Hamburg University of Technology (TUHH), Eißendorfer Straße 40, 21073 Hamburg, Germany

ARTICLE INFO

Keywords:
Variable stiffness composites
Automated composite design
Automated Fiber Placement (AFP)
Variable-angle tow laminates
Curvilinear fiber paths
Robot-assisted manufacturing
Global optimization

ABSTRACT

In the aerospace sector, weight reduction is crucial for enhancing performance and efficiency. Significant advantages of using Carbon Fiber Reinforced Polymer (CFRP) in structural designs include the weight saving potential by leveraging their favorable strength-to-weight and stiffness-to-weight ratios, as well as their ability to modulate properties through strategic laminate design. Traditional composite design methods often depend on constant-stiffness, utilizing quasi-isotropic layouts with uniform fiber orientation angles across each layer. Although this method preserves structural integrity, it does not fully leverage the potential of advanced composite materials and fiber placement technologies for weight minimization. Introducing variable fiber directions can achieve further weight reductions. However, this expanded design flexibility introduces new challenges and necessitates automation in the design process. This paper builds on these concepts, presenting a novel approach to structural design using Variable Angle Tow (VAT) laminates for Automated Fiber Placement (AFP) manufacturing. Specifically tailored for complex double-curved components, this method aims to optimize weight and reduce manual effort while simultaneously maintaining or enhancing structural performance and ensuring manufacturability. It encompasses an automated nested loop optimization process utilizing Finite Element Analysis (FEA) and algorithmic design to fine-tune the orientation and curvature of splines, as well as the thickness of individual layers, thereby achieving mass reduction. The entire process effectively bridges the gap between design and manufacturing, from the initial CAD model import of the part surface to the generation of executable robot control code. The method is applied to a 2D plate and a double-curved 3D wing shell under exemplary loading conditions. Weight reductions of up to 7.44% were achieved compared to classical laminates. These exemplary results, while dependent on specific components and load cases, demonstrate the efficacy of the method and the potential for weight savings in aerospace structures.

1. Introduction

The adoption of new technologies is crucial for the aerospace industry for reducing aircraft weight, which is essential for better fuel efficiency and increased payload capacity. The demand for materials that offer high strength-to-weight ratios, as well as corrosion and fatigue resistance, has led to the widespread adoption of composites in aerospace applications [1]. In aerospace applications, unidirectional materials with continuous fibers are predominantly used. These fibers are fixed in the desired geometry by a matrix material or resin after curing for thermosets or consolidation for thermoplastics, forming layers called laminae that are stacked in a specific sequence to create a laminate. Unlike isotropic metallic materials, which are characterized by directionally independent elastic properties, unidirectional laminae are orthotropic and exhibit directionally dependent properties within the plane of the layer. The mechanical behavior of laminated composites is significantly influenced by factors such as fiber orientations, stacking sequences, and ply thickness. These parameters can be optimized to design composite structures that meet specific requirements [2]. Fiber-reinforced laminate composites like Carbon Fiber Reinforced Polymer

☆ This research was funded by dtec.bw – Digitalization and Technology Research Center of the Bundeswehr. dtec.bw is funded by the European Union – NextGenerationEU.

* Corresponding author at: Helmut Schmidt University Hamburg, Holstenhofweg 85, 22043 Hamburg, Germany.
E-mail address: pezhman.pourabdollah@airbus.com (P. Pourabdollah).
URL: https://www.hsu-hh.de/aut/team/pourabdollah (P. Pourabdollah).

https://doi.org/10.1016/j.compstruct.2025.119511
Received 14 February 2025; Received in revised form 20 June 2025; Accepted 22 July 2025
Available online 31 July 2025

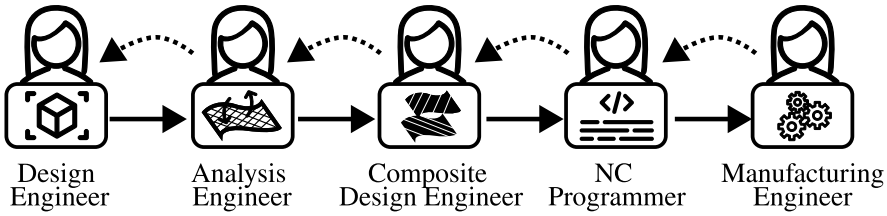

Fig. 1. Illustration of the design process for CFRP components manufactured with AFP showing the fragmented workflow and iterative loops in aerospace applications.

(CFRP) are extensively used in the Boeing 787 and Airbus A350-XWB, making up over 50 wt%, improving both secondary and primary aircraft structures [1,3].

Various automated and semi-automated fiber placement methods are used in aerospace, with Automated Fiber Placement (AFP) and Automated Tape Laying (ATL) being the most common. Lukaszewicz et al. discuss the historical developments and technological advancements of AFP and ATL technologies in their review [3]. Increasingly, the industry is shifting from ATL to AFP due to its technological advantages [4]. Notably, studies by Lukaszewicz have shown AFP to be more efficient across different component sizes [5,6]. An AFP system uses a robotic arm or gantry configuration with a placement head to deposit pre-impregnated carbon fiber tows. The fiber placement head utilizes integrated heating and a compaction roller to bond the tows securely to the base or previous layers, building the part additively until the desired geometry is reached. AFP increases precision, consistency, speed, and allows for curved fiber placement within the plane of the layer. For a broad review of AFP systems the interested reader is referred to [7,8]. Continuous Tow Shearing and Rapid Tow Shearing are more recent approaches to deposit fiber material that reduce fiber buckling and wrinkling by using shear deformations instead of bending forces, allowing for a smaller steering radius. However, these methods are limited to 2D fiber placement, requiring extra steps for 3D components. Additionally, shearing can cause significant variations in part thickness, which may accumulate and lead to undesired effects [9,10].

The overall design process for CFRP components manufactured with AFP in the aerospace industry lacks continuity and requires numerous manual steps and interpretations. As illustrated in Fig. 1, the process spans multiple disciplines such as design, analysis, composite design, NC programming, and manufacturing, which largely operate as knowledge silos. These disciplines utilize different software applications, and interfaces between the software of various disciplines are non-existent. Iterative loops between these instances are frequently necessary, altering the design and consequently the laminate structure. Each iteration requires compromises, further complicating the process. This fragmented approach not only hampers efficiency, but also potentially impacts the quality and consistency of the final CFRP components.

Effective composite design integrates both geometry and fiber ply design [11]. Ghiasi et al. categorize composite design into Constant Stiffness (CS) [12] and Variable Stiffness (VS) [13] designs. The conventional approach to composite material design, known as CS laminates, relies on quasi-isotropic layouts with consistent fiber orientation per layer. CS laminates are integral to aircraft manufacturing and are used to ensure uniform stiffness. Aircraft manufacturers employ composite design rules that simplify both construction and load calculations, ensuring that materials meet stringent safety and performance requirements for aircraft. These rules include using classical layer orientations ($-45°/45°/90°/0°$) and designing laminates to be symmetrical and balanced, which minimizes mechanical coupling effects and promotes even stress distribution. The proportion of each orientation should be at least 10%, allowing the material to effectively handle loads from various directions without being too stiff or too flexible in any one direction [14]. Furthermore, the strategic positioning of $-45°/45°$ fiber pairs as the outermost layers provides a protective function for the underlying plies [15]. Optimizing CS laminates involves determining the optimal number of layers, set of fixed fiber orientations, stacking sequence and thickness to achieve performance objectives such as in-plane strength, buckling load, flexural stiffness, and natural frequency [16–20]. For a comprehensive review of CS laminate design methodologies, the reader is referred to [12]. While this approach ensures structural integrity, it fails to fully exploit the potential of composite materials and modern manufacturing techniques, particularly the capabilities of fiber placement machines, hindering full utilization of the material's directional properties.

In contrast, VS laminates have spatially varied stiffness to tailor stress distribution for enhanced structural performance. Techniques to achieve this variability include combining various CS laminates across different structural zones or using curvilinear fiber paths, known as Variable Angle Tow (VAT) laminates. The use of AFP machines gives the freedom to tailor the properties in directions that are more favorable for carrying loads within the laminate. This approach expands design capabilities and enhances mechanical properties and efficiency but adds complexity, requiring automated design and precise path planning in AFP processes to manage potential manufacturing defects.

Heinecke et al. have outlined various defects such as gaps, overlaps, tow wrinkling, bridging, and crowning that can occur during manufacturing with the AFP process [21]. Manufacturing constraints such as minimum radius and spacing requirements can have a decisive impact on tow-steered laminate optimization and should therefore be integrated from the start [22]. Sawicki and Minguett demonstrated that a gap of 0.76 mm could reduce the compressive strength of a laminate by up to 27% [23]. Croft et al. concluded in a study that overlap could reduce in-plane shear strength by up to 13% [24]. Recent findings confirm that overlap and gap defects in tow-steered laminates significantly affect buckling strength, highlighting the importance of defect-free fiber placement [25]. Depending on the AFP machine, material, and process parameter settings, different minimum layup radii can be achieved. Various values are reported in the literature. For example, Füssel et al. reported a minimum layup radius of 50 mm using a thermoplastic polymer with short fibers [26]. However, thermoset materials and long fibers require a larger radius to ensure defect-free manufacturing. It is important to emphasize that the minimum layup radius is not only dependent on the material but also influenced by the specific AFP machine, the component being manufactured, and various process parameters.

VAT laminates have shown significant improvements in structural performance compared to traditional straight fiber designs. Studies have demonstrated that VAT panels can achieve up to 20% weight savings when optimized for buckling performance [27]. One early demonstration of this was provided by Hyer and Lee, who showed that curvilinear fiber paths can significantly improve buckling resistance in composite plates with central circular holes [28]. Furthermore, many researchers have found that VS laminates exhibit stiffer post-buckling behavior than their straight fiber counterparts, as exemplified by Groh and Weaver [10]. For instance, Aoki et al. reported that composites with curved fibers exhibit a 6% higher initial failure load and 3% higher panel stiffness [29]. The concept of utilizing curvilinear fiber deposition to enhance the effectiveness of fiber-reinforced materials has been explored since the 1970s. Brandmaier demonstrated

that the optimal orientation of fibers for maximizing the mechanical strength of composites is not inherently aligned with the principal stress directions, but rather depends on the distinct strength properties inherent to the individual layers of the laminate [30]. This finding was further developed to analyze the effect of fiber curvature on mechanical properties [31,32]. Since then, numerous optimization approaches have been developed to leverage the advantages of curvilinear fiber paths [33–36]. Many continue to use principal stress directions to align fibers, as Hyer and Charette demonstrated in the study [37]. Others utilize lamination parameters to generate VAT fiber paths [38,39]. The optimal alignment of variable fiber angles depends on the loading and boundary conditions. The extensive design possibilities inherent to VAT laminates present intricate challenges in structural optimization [40].

Over the past decade, the specialized areas of VS and topology design in laminated composites have required significantly more design resources than CS laminate optimizations [11]. Due to the vast number of design variables, manually optimizing laminate configurations is highly challenging. To address this complexity, it is necessary to develop optimization strategies that effectively explore the design space. The performance improvements possible with VS laminates are constrained by the capabilities of AFP technology. Thus, manufacturability must be incorporated into the design process to ensure that the designs are both practical and achievable within existing technological constraints.

While significant progress has been made in optimizing VAT laminates, several critical gaps remain in the current state of research. Many studies focus on structural optimization without adequately considering manufacturability constraints, often addressing these limitations only in later design stages [41]. This approach can lead to optimal designs, but they may require subsequent adjustments, causing deviations from the original optimum. The emphasis on structural optimization without manufacturing considerations has resulted in few practical applications for VAT laminates. For example, Setoodeh et al. used lamination parameters in a two-level optimization strategy to design a VAT laminate, which resulted in discontinuous curvilinear fiber paths [42]. Although some studies have attempted to address this issue, they frequently neglect other critical manufacturabiltiy aspects, lacking holistic approaches that simultaneously consider multiple factors such as minimum curvature radius, gaps, and overlaps. For instance, Montemurro and Catapano developed an optimization strategy for VAT laminates that considers minimal layup radii but overlooks gaps and overlaps, resulting in theoretical optima that are not manufacturable [43]. Furthermore, like many studies, the approach is limited to 2D applications and fails to account for the complexity of real 3D components. Notably absent from most studies is an end-to-end process chain directly linking optimization and design to laminate manufacturing, creating a significant gap between theoretical designs and practical implementation. Recent work by Noevere et al. has addressed the need for a comprehensive process chain in developing laminates for AFP manufacturing [44]. However, their method, while offering a more comprehensive workflow, lacks automated optimization and design generation. Additionally, their focus is primarily on adapting fixed fiber orientations to curved surfaces rather than exploring the full potential of VAT designs. This discrepancy between theory and practice underscores the need for an integrated approach that considers both structural performance and manufacturing constraints from the outset of the design process, while allowing for more innovative fiber orientation strategies beyond traditional fixed angles.

In conclusion, the design and manufacturing of composite structures for aerospace applications require an advanced optimization process that addresses current limitations. Key requirements encompass the integration of manufacturing constraints from the design outset and full automation capable of handling 2D and 3D components of any scale. The process must incorporate AFP considerations such as minimum curvature radius, gaps, and overlaps while optimizing structural performance and weight. It should explore innovative fiber orientation strategies and provide a seamless workflow from design to manufacturing. This paper proposes an innovative, nested loop optimization process for designing CFRP laminates for AFP manufacturing. The method utilizes VAT technology, adjusting both ply design and layer thickness to maximize weight savings while maintaining structural integrity. This comprehensive approach offers precise control over material properties within manufacturing constraints, aiming to enhance the practical applicability of VAT laminates in complex aircraft structures. By addressing the identified requirements, this methodology seeks to improve the effective use of advanced materials and AFP techniques in aerospace, potentially leading to optimized performance and increased efficiency in aircraft design and manufacturing.

The remainder of the paper is structured as follows. Section 2 presents a nested loop optimization method aimed at weight reduction and structural integrity enhancement of the composite laminates, including an automated design process for VAT laminates in Section 2.1. Section 2.2 addresses the manufacturability analysis considerations and challenges associated with AFP, detailing the strategies employed to incorporate these elements into the laminate design. To facilitate readability, necessary fundamentals for each part of the concept are explained at the beginning of the respective chapters. The numerical results of the proposed optimization process, including an academic example featuring a rectangular 2D plate, and a practical application of a double-curved 3D shape representative of a wing shell of a commercial aircraft, are presented in Section 3. Finally, Section 4 summarizes the key outcomes of this research and proposes directions for future work.

2. Automated VAT laminate design generation and optimization methodology

In this study, a nested loop optimization workflow is developed, as illustrated in Fig. 10. Both optimizers target the minimization of structural weight as their primary objective. The first optimizer uses the control points of the Non-Uniform Rational B-Spline (NURBS) curve (see Section 2.1.1) as design variables in a black-box optimization algorithm. This curve also serves as the reference for the VAT propagation that creates a ply (see Section 2.1.2). The second optimizer targets the thickness of each layer in the laminate design as its design variables through a gradient-based optimization algorithm. The workflow was developed using Rhinoceros 3D (Rhino) Grasshopper. The first optimizer was implemented in Python, while Altair's OptiStruct was utilized for the second optimizer.

The proposed methodology employs a nested-loop optimization framework with two optimizers, as illustrated in Fig. 2. It integrates VAT layers with conventional ply orientations, as shown in Fig. 3 , to create weight-optimized and manufacturable laminate designs compatible with AFP processes. The two optimizers operate in combination to minimize structural mass, with the outer loop defining the global fiber path and the inner loop refining the laminate thickness distribution. In the outer loop, a black-box optimization algorithm adjusts the control points of a NURBS reference curve (see Section 2.1.1). This curve also serves as the reference for the VAT propagation that creates a ply (see Section 2.1.2). By guiding fibers along paths that reflect the structural requirements, the stiffness-to-mass ratio is improved. After each update of the fiber path, manufacturability checks ensure that no steering-induced defects are introduced. Only designs meeting these requirements proceed to the inner loop. In the inner loop, a gradient-based optimization algorithm refines the discrete layer thicknesses, typically specified as integer multiples of the employed ply thickness. This step further reduces mass without compromising mechanical performance. Once thickness optimization is complete, stopping criteria are evaluated to determine whether further refinements are necessary. The resulting methodology provides a fully optimized VAT laminate configuration that refines both fiber paths and laminate thicknesses. This ensures that the final design is both mass-efficient and compatible with AFP, offering a practical approach to improving the structural performance of advanced composite laminates. In the following, the different steps of the workflow are explained in detail.

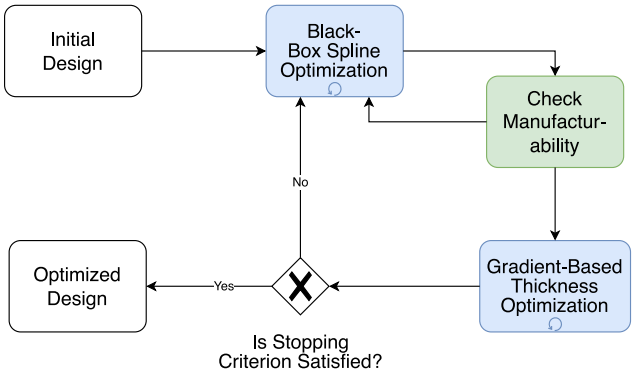

Fig. 2. Simplified overview of the automated design generation and optimization workflow for variable angle tow laminates. In this work, RBFOpt is used for the black-box spline optimization and OptiStruct is used for the gradient-based thickness optimization.

2.1. VAT ply design generation

The proposed design generation process begins by defining a reference curve for each VAT ply. This curve serves as the foundation for creating additional fiber paths that collectively form a single layer. It is later used for tow replication strategies to cover the desired surface with paths.

2.1.1. Reference curve

For the construction or selection of a reference curve, the following requirements should be met. First, the parametrization should prioritize flexibility while maintaining a minimal parameter count to enable the use of a black-box optimizer. The parametrization should be able to describe fundamental path types such as C-curves (single curvature), and S-curves (double curvature). Furthermore, the reference curve must extend beyond the component's boundaries to ensure complete coverage during the offset process. When the reference curve does not fully span the component, the resulting offset must be artificially extended. While many algorithms, including the one described by Qu et al. [45], address the need for curve extensions, the most typical approach is either appending a linear segment or extrapolating the terminal curvature. However, both approaches introduce abrupt transitions that fail to capture the complex curvature variations of the component. In particular, linear extensions disrupt curvature continuity, while merely continuing the terminal curvature ignores local geometric nuances. As a result, these methods often lead to suboptimal integration with the component's overall design.

In the present paper, the reference curve is constructed as a NURBS curve $\mathbf{C}(u)$ within the xy-plane and is then projected onto the double-curved surface of the component. This curve offers great design flexibility with only a few adjustable variables, making it ideally suited for creating VAT layer designs. Compared to the iso-contour-based method proposed by Arsenyeva et al. [46], which generates fiber paths indirectly via artificial guiding surfaces, our approach provides direct geometric control through NURBS projection and offsetting. This ensures robust AFP-compatible layup generation even on double-curved geometries and enables precise control over fiber spacing and curvature.

The NURBS curve $\mathbf{C}(u)$ is mathematically defined through the weighted sum of control points $\mathbf{P}_i = (x_i, y_i)$ and the associated rational B-spline basis functions $R_{i,k}(u)$, where k is the B-spline degree and u is the path coordinate. A curve with n control points is given by:

$$\mathbf{C}(u) = \sum_{i=0}^{n} R_{i,k}(u)\mathbf{P}_i \tag{1}$$

In this implementation, cubic B-splines (k = 3) are employed. The workflow for generating the reference curve begins by projecting the component's geometry onto the xy-plane and creating two concentric circles with the centeroid of the projection at their center. The first circle encompasses the projection, while the second circle has a larger radius and is used to define the start and endpoints of the initial spline. This ensures that the start and end points of any offset curve lie outside the boundaries of the component.

Six points $\mathbf{P}_1, \mathbf{P}_2, \mathbf{P}_3, \mathbf{P}_4, \mathbf{P}_5$ and $\mathbf{P}_6$ are created using these circles, which serve as control points for a NURBS spline, as shown in Fig. 4. The first point $\mathbf{P}_1$ can be positioned anywhere on the outer circle using the variable x_1. The second point $\mathbf{P}_2$ is linearly dependent on the first and is the symmetric counterpart of the first with respect to the center of the circle. The points $\mathbf{P}_3$ and $\mathbf{P}_4$ on the inner circle are those with the shortest distance to $\mathbf{P}_1$ and $\mathbf{P}_2$ respectively and are therefore also dependent on the first point. Another control point $\mathbf{P}_5$ is determined using the center point $\hat{\mathbf{P}}_5$ of the line that connects $\mathbf{P}_1$ and $\mathbf{P}_2$. $\mathbf{P}_5$ is positioned orthogonal to this line using the variable x_2. The last control point $\mathbf{P}_6$ is generated using the point $\hat{\mathbf{P}}_6$, which is positioned on the second half of the line and can move along this segment. The variable x_3 controls the position between the center point $\hat{\mathbf{P}}_5$ of the line and the end point $\mathbf{P}_1$, and the variable x_4 changes the position orthogonal to the line, resulting in $\mathbf{P}_6$. In total, the NURBS curve is therefore shaped by six control points (the red dots in Fig. 4), which can be controlled by the four variables combined as the vector $\mathbf{x} = \begin{pmatrix} x_1 & x_2 & x_3 & x_4 \end{pmatrix}^T$ (the green arrows in Fig. 4).

The four variables (x_1, x_2, x_3, x_4) that parameterize the six control points ($\mathbf{P}_1$ through $\mathbf{P}_6$) as detailed above, serve as the primary design parameters for the subsequent spline shape optimization. They define the initial reference spline and consequently the overall spline configuration of the entire VAT ply.

The initial spline design is highly flexible, using four variables to transform it into various shapes, from simple straight lines to C-shaped or S-shaped curves. Adjusting the control points' positions and orientations gives precise control over the spline, allowing it to meet specific design requirements. The minimization of variables in an optimization problem is crucial because computational complexity is reduced, efficiency is increased, and the likelihood of identifying an optimal solution is improved [47]. Once configured, the NURBS spline is projected onto the 3D surface $\mathbf{S}(u, v)$ of the part, transforming it into a three-dimensional spline $\mathbf{Q}(u)$. This seamless integration maintains the curve's geometric properties within the model's three-dimensional structure. The projection of the NURBS curve $\mathbf{C}(u)$ onto a 3D surface $\mathbf{S}(u, v)$ is achieved by finding the corresponding parameters $v = v(u)$, such that the points of the curve are mapped onto the surface:

$$\mathbf{Q}(u) = \mathbf{S}(u, v(u)) \tag{2}$$

2.1.2. Tow replication strategies

There are several layup strategies for configuring curved fiber paths. These can be developed using either the shifted or offset (parallel) methods, as shown in Fig. 5. In the shifted method, the reference curve is moved in one direction to cover the entire ply area. In contrast, the offset method places all fiber paths in a ply parallel to the reference curve.

The offset curve strategy is the most commonly used method for path planning, though many publications use a simple shift of the reference curve to achieve coverage [48]. The shift method can create issues such as overlaps and variable tow distances due to the large curvatures of the initial curve, leading to variations in fiber volume fraction and uneven laminates. Conversely, the offset method arranges all additional fiber paths exactly parallel to the reference curve, maintaining consistent distances between paths. However, this causes the curvature of the paths to change with each offset, potentially becoming

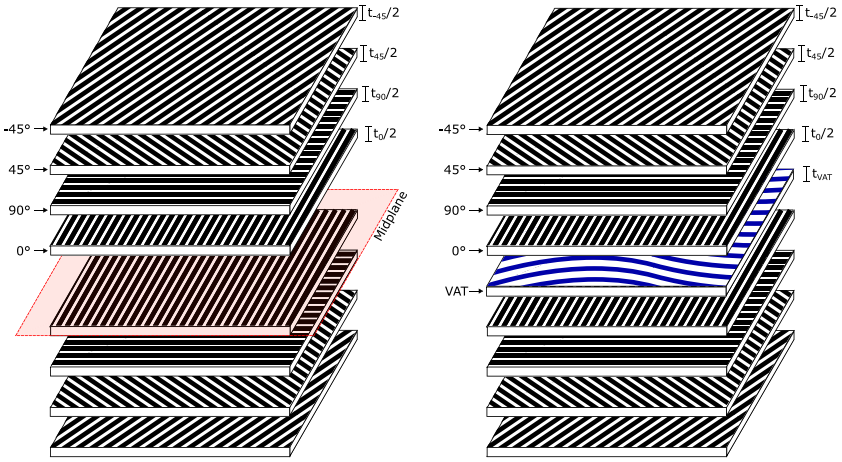

Fig. 3. Configuration of a symmetric laminate, illustrated as an exploded view showing distinct ply groups on one side of the midplane. The design variables t_{-45}, t_{+45}, t_{90}, and t_0 represent the total thickness for each respective ply group ($-45°, +45°, 90°$, and $0°$) within one symmetric half of the laminate, while t_{VAT} denotes the total thickness of the centrally positioned VAT layer. For clarity in the exploded view, each depicted segment of a standard orientation ply group is labeled with half of its corresponding design variable. (a) Layer arrangement for a standard CS laminate. (b) VS laminate with a VAT layer of total thickness t_{VAT} positioned at the midplane.

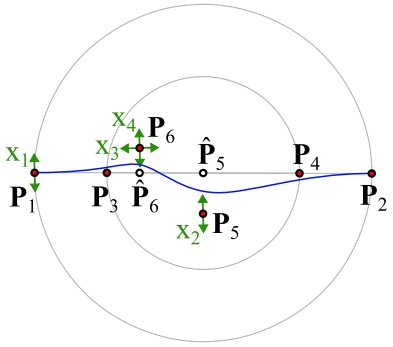

Fig. 4. Schematic representation of the NURBS spline generation process for VAT laminate design. Displaying the placement and configuration of control points on two concentric circles.

too pronounced and complicating the calculations, especially in three-dimensional space, as described by Takashi in [49]. Mathematically, an offset is not always straightforward, especially in areas where the original curve is highly curved. The challenge lies in the fact that if the offset radius is too small compared to the radius of curvature of the original curve, self-intersections or discontinuities can occur in the offset curve [50,51]. Furthermore, in some publications, offsets are used but are performed in 2D and then projected onto a double-curved 3D surface, e.g., Tanaka et al. in [52], which results in paths that are not equidistant on the surface.

In the aerospace industry, where uniformity and precision are essential, the avoidance of manufacturing defects such as gaps and overlaps is viewed as critical. In light of these considerations, the offset method has been selected as the tow replication strategy for the approach described in this paper. By performing the offset calculation on the actual 3D surface, consistent inter-tow spacing is maintained even on highly curved geometries. The 3D offset method addresses the limitations of 2D approaches and provides a more robust solution for designing variable stiffness laminates on complex, double-curved surfaces. By maintaining consistent spacing between fiber paths, this method is not only aligned with industry standards but is also expected to provide a robust foundation for optimizing structural performance and manufacturing efficiency.

2.2. Manufacturability analysis

The AFP manufacturing method offers numerous advantages, yet it also has inherent limitations that designers must consider. This approach involves incorporating manufacturability constraints directly into the process of VAT laminate design generation. This is as crucial as optimizing mechanical properties, ensuring that the optimized design is feasible for real-world production. In AFP, there are principally three main tow steering defects: tow buckling, tow pull-up, and tow misalignment [3]. Tow buckling typically occurs on the inside radius of a tow if compressive forces are too high, while tow pull-up occurs on the outside of a tow due to excessive tensile forces [24]. Twisted tows can also occur but are less common [53]. Different studies emphasize the importance of considering the smallest possible steering radius as a critical factor in defect development [54–56].

To avoid the above-mentioned defects, this approach integrates the manufacturability criteria from the onset of path generation to ensure that only feasible paths that meet production standards are created. This manufacturability analysis, which builds upon the pre-analysis, post-analysis, and the handling of sub-minimal paths, comprehensively addresses the manufacturing constraints. By acknowledging and addressing the limitations of AFP through these multiple analytical steps, this approach ensures both the feasibility and the integrity of the manufactured aerospace components.

2.2.1. Pre-analysis of path viability

The pre-analysis for curvature determination, developed as part of this methodology, uses an algorithm that predicts where the curvature radii will become minimal, based on the initial spline $\mathbf{C}(u)$, and thus could potentially lead to discontinuities or non-manufacturable small radii in the offset paths. This approach allows for adjustments to be made before generating the paths to identify and eliminate non-manufacturable paths early on. As a result, the entire design process is made more efficient, since additional computationally intensive calculations of unfeasible offset paths are avoided.

The curvature radius $r(u)$ is determined from the differential geometry of the curve:

$$r(u) = \frac{\|\mathbf{C}'(u)\|^3}{\|\mathbf{C}'(u) \times \mathbf{C}''(u)\|} \tag{3}$$

The analysis focuses on the concave offset of the curve, as the curves in these areas have a greater curvature than the initial curve and are therefore potentially more challenging to manufacture. The

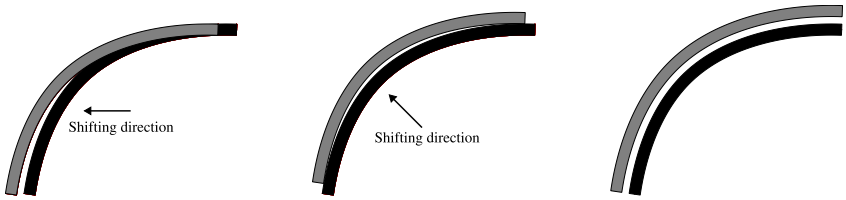

Fig. 5. Comparison of fiber path layup strategies for variable stiffness laminates. (a) Shifted method in the −x direction, (b) Shifted method in the −x and +y directions, (c) Offset method.

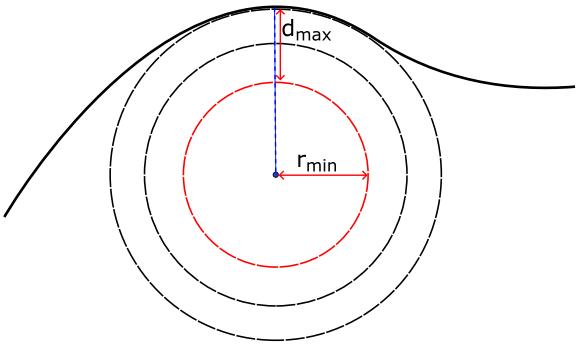

Fig. 6. Illustration of the pre-analysis of path viability in laminate path design.

relationship between the radii of the original and the offset curve can be expressed by the formula:

$$r_2 = r_1 - d \tag{4}$$

where r_1 represents the curvature radius of the initial curve and r_2 represents the curvature radius of an offset curve with the offset distance d from the initial curve. The curvature $\kappa_{i,j}$ at a specific point i on the curve $\mathbf{c}_j$ is determined by the reciprocal of the radius $r_{i,j}$ of the circle that best approximates the curve $\mathbf{c}_j$ at the desired point i according to the equation:

$$\kappa_{i,j} = \frac{1}{r_{i,j}} \tag{5}$$

Although this estimation method employs a 2D analysis, which may be less precise for highly curved components, it has demonstrated adequate accuracy for the tested 3D geometries.

Thus, the maximum offset distance $d_{max} = r_1 - r_{min}$ is the distance up to which an offset curve can be generated without exceeding the minimum bending radius r_{min}, as illustrated in Fig. 6.

The specific algorithmic procedure for this pre-analysis of path viability is visualized in Fig. 7. This flowchart details how critical points $P_{Cmin,i}$ with local minimum radii $r_{Cmin,i}$ are identified on the reference curve. Given that the reference curve generation method (Section 2.1.1) primarily produces C- or S-shaped curves, the algorithm typically identifies one such critical point for C-shaped paths and two for S-shaped paths. For each of these identified points, the pre-analysis calculates a critical inward offset distance $d_{max,i}$. This $d_{max,i}$ is subsequently used to project $P_{Cmin,i}$ in its concave direction to a test point $P_{offs,i}$, which represents the critical location where the minimum offset radius r_{min} would be violated. At this test point $P_{offs,i}$, the resulting radius becomes smaller than the allowable r_{min}, thereby indicating a non-manufacturable condition. The manufacturability of the path segment related to $P_{Cmin,i}$ is then determined by evaluating whether this test point $P_{offs,i}$ lies within the part boundaries or if any further offsetting from $P_{offs,i}$ would cause the path to re-enter the part geometry. A failure at any critical point results in the entire reference curve being deemed non-manufacturable, which then triggers a penalty for Optimizer I, as detailed later.

The algorithm evaluates the initial curve using circles that match its curvature. Replication and further calculations are terminated under two specific conditions. First, if a point is identified within the component boundaries where the curvature exceeds the permissible limit or a discontinuity occurs. Second, if a point outside the component boundaries is found whose replication would result in non-manufacturable curves within the component boundaries. In either of these scenarios, the algorithm bypasses subsequent steps and reports the mass of an optimized standard laminate back to the optimizer. This action serves as a direct penalty mechanism within the optimization loop: Optimizer I receives the mass value of an optimized standard laminate (as a baseline reference) for any set of design variables (x_1, x_2, x_3, x_4) that leads to such a non-manufacturable path according to this pre-analysis. Consequently, Optimizer I is guided to avoid regions in the design space that produce paths violating the minimum curvature radius (r_{min}). This integration ensures that only designs passing this curvature check proceed to the inner loop for evaluation by Optimizer II.

More efficient algorithms allow for more iterations and a broader range of design possibilities within the same timeframe and computing power constraints. This approach eliminates the necessity for time-consuming calculations of unfeasible paths, thus enhancing the efficiency of the overall design and optimization process by estimating manufacturability based solely on the initial spline. However, it is important to note that a final, exact verification of curvature must be conducted on the final design to confirm the manufacturability of all curves.

2.2.2. *Post-analysis of path viability*

The post-analysis procedure serves as a critical final validation step for all generated curves, encompassing both the initial and any offset curves. This process is designed to meticulously examine each curve for discontinuities and to verify that the curvature remains within the predefined limits established by the maximum allowable curvature. The procedure involves two key steps:

- Discontinuity Detection: Each curve is analyzed for any abrupt changes or breaks that could compromise the integrity of the fiber placement.
- Curvature Analysis: The point of highest curvature on each curve is identified and evaluated against the maximum allowable curvature. This critical value, denoted as κ_{max}, is determined by the specific AFP machine capabilities and the material properties of the composite fibers.

Mathematically, for a curve $\mathbf{c}_j$, the curvature κ_i at any point is given by:

$$\kappa_i = \frac{|\mathbf{c}'_j \times \mathbf{c}''_j|}{|\mathbf{c}'_j|^3} \tag{6}$$

where $\mathbf{c}'_j$ and $\mathbf{c}''_j$ are the first and second derivatives of the curve with respect to u.

The post-analysis ensures that for each curve $\mathbf{c}_j \in C$:

$$\max \kappa_i \leq \kappa_{max} \tag{7}$$

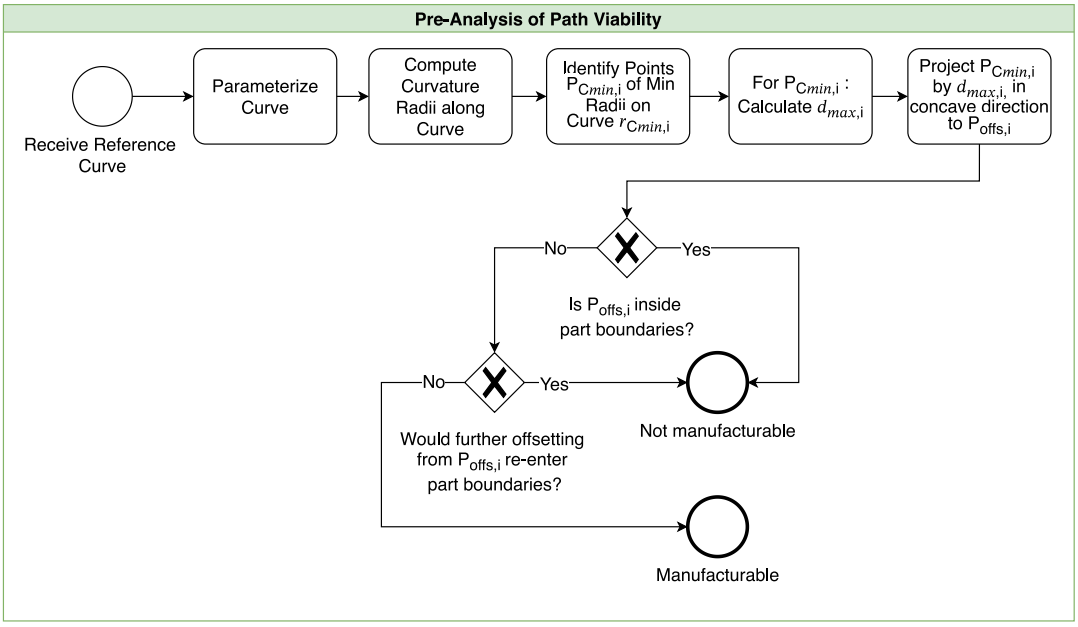

Fig. 7. Detailed flowchart of the pre-analysis of path viability algorithm. For each identified local minimum curvature point ($P_{Cmin,i}$), the process depicts the generation of an offset test point $P_{offs,i}$ (at which the offset radius would be r_{min}) and its evaluation against part boundaries, including re-entry checks.

It is important to note that this post-analysis method is not incorporated within the iterative optimization loop due to its computationally intensive nature, as it requires generating paths for the entire component. Instead, it serves as a final verification step for the optimized set of curves, which are derived from the reference curve that was already examined in the pre-analysis, before they are sent to the AFP machine for manufacturing.

Instead, it serves as a crucial final verification step for the ultimately selected, optimized set of curves C before they are sent to the AFP machine for manufacturing.

The importance of this post-analysis is especially apparent in scenarios involving components with substantial curvature. For such highly curved parts, the initial pre-analysis estimations might mistakenly deem certain paths as manufacturable. However, these paths may in fact surpass the capabilities of the machinery or the limitations of the materials used.

2.2.3. Handling of sub-minimal paths

During the path generation process, certain curves might be produced that are shorter than the minimal cutting length required for manufacturing. These sub-minimal curves pose challenges to manufacturability and can potentially affect the structural integrity of the component. To address this issue, an approach for handling such curves was implemented.

Let L_{min} be the minimum cutting length required by the AFP machine, and $C = \{\mathbf{c}_1, \mathbf{c}_2, \ldots, \mathbf{c}_m\}$ be the set of generated 3D curves. For each curve $\mathbf{c}_j \in C$, the length of the curve is defined as $l(\mathbf{c}_j)$. The set of sub-minimal curves C_{sm} is identified as:

$$C_{sm} = \{\mathbf{c}_j \in C : l(\mathbf{c}_j) < L_{min}\} \tag{8}$$

The operator can decide which strategy to pursue for handling these sub-minimal curves, based on specific design requirements and manufacturing constraints. Two primary strategies are available:

1. Curve Extension: This strategy is chosen when complete surface coverage is necessary, for example, to ensure consistent force distribution in the area or to maintain uniform component thickness. For each curve $\mathbf{c}_s \in C_{sm}$, the extension Δl is calculated as:

$$\Delta l = L_{min} - l(\mathbf{c}_s) \tag{9}$$

The extension is applied to one end of the curve, maintaining the same angle as the original curve, until the minimum cutting length is achieved. However, it is important to note that this method results in fiber placement beyond the final component contour, necessitating a subsequent trimming operation to achieve the desired final shape.

2. Curve Removal: In scenarios where strict adherence to the original design, meaning placement closer to the final component contour, is prioritized over complete coverage, the operator may choose to remove sub-minimal curves. This option might be preferred in areas of low stress or where slight variations in thickness are acceptable. This approach can potentially reduce or eliminate the need for trimming operations, resulting in a more efficient manufacturing process and less material waste.

In Fig. 8, the left section displays curves at the component edge with non-manufacturable paths in red. The middle section shows extended paths to the minimum layup length, highlighted in green, while the right section illustrates the removal of paths below this threshold.

The decision between curve extension and curve removal is made by the operator for the finalized, optimized design that results from the completed optimization loop. This handling of sub-minimal paths is therefore considered a post-processing step. The operator's choice is based on a comprehensive analysis of the selected optimal design, considering factors including local geometry, load distribution, specific manufacturing constraints of the project, and the trade-off between ensuring complete coverage versus minimizing subsequent trimming or material wastage. Since this procedure is applied after the entire optimization process has concluded, it does not influence the iterative search performed by Optimizer I or the thickness adjustments made by Optimizer II during the optimization run.

2.3. VAT orientation mapping algorithm

The VAT orientation mapping algorithm is designed to translate continuous curve data into discrete angular values for mesh elements. This process enhances the mesh's capability to capture the geometric fidelity of the original VAT design. The algorithm operates on a set of 3D curves generated through an offset procedure, explained in

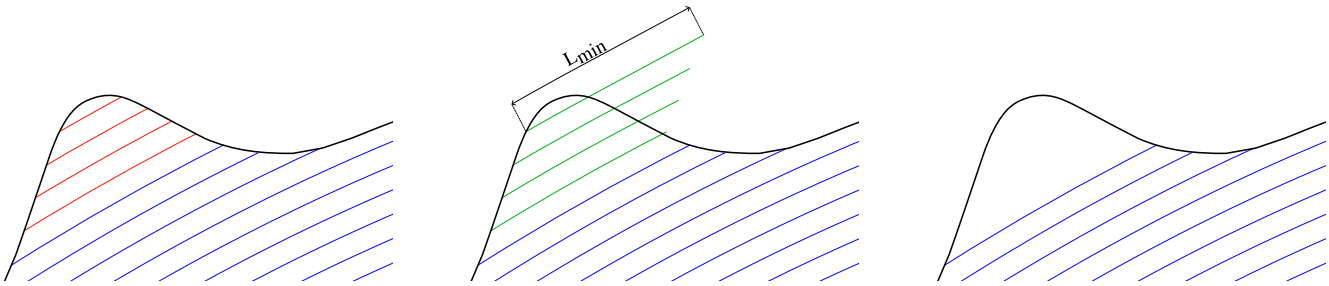

Fig. 8. Left: Initial curves with non-manufacturable segments highlighted in red. Middle: Curves extended by the algorithm to meet minimum layup length highlighted in green. Right: Removal of sub-minimal curves.

Section 2.1.2, which collectively cover the entire surface of the component and represent the centerlines of AFP tows within a continuous geometry. The computed orientation angles θ_i are written into the drape-table section of the `.fem` file, ensuring that each finite element carries its assigned fiber orientation into the solver.

The assignment of an orientation angle to each finite element $\mathbf{e}_i$ from the set of mesh elements $E = \{\mathbf{e}_1, \mathbf{e}_2, \ldots, \mathbf{e}_n\}$, based on the set of 3D curves $C = \{\mathbf{c}_1, \mathbf{c}_2, \ldots, \mathbf{c}_m\}$, follows a defined sequence. Initially, for each element $\mathbf{e}_i$, its geometric centroid $\mathbf{p}_i$ is determined. Subsequently, the algorithm identifies the specific curve $\mathbf{c}_j \in C$ that minimizes the Euclidean distance d between the element's center point $\mathbf{p}_i$ and the curve:

$$\mathbf{c}_j = \underset{\mathbf{c}\in C}{\operatorname{argmin}} \sqrt{(x_c - x_{p_i})^2 + (y_c - y_{p_i})^2 + (z_c - z_{p_i})^2} \tag{10}$$

where $\mathbf{c}_j$ is the selected curve, C is the set of all curves, (x_c, y_c, z_c) are the coordinates of a point on curve $\mathbf{c}$, and $(x_{\mathbf{p}_i}, y_{\mathbf{p}_i}, z_{\mathbf{p}_i})$ are the coordinates of the center of element $\mathbf{e}_i$. At the point of minimum distance $\mathbf{p}^*$ on curve $\mathbf{c}_j$, the algorithm computes the tangent vector:

$$\vec{T} = (T_x, T_y, T_z) \tag{11}$$

The projection of this tangent vector onto the global xy-plane dictates the fiber orientation within the lamina. The orientation angle θ_i for element $\mathbf{e}_i$ is then determined using the x and y components of $\vec{T}$:

$$\theta_i = \operatorname{atan2}(T_y, T_x) \tag{12}$$

where atan2 is the two-argument arctangent function, which returns the angle in the correct quadrant. This process is repeated for all elements in the mesh, resulting in a mapping function

$$\boldsymbol{\Phi} : E \to \mathbb{R} \tag{13}$$

that assigns an orientation angle to each element:

$$\boldsymbol{\Phi}(\mathbf{e}_i) = \theta_i \tag{14}$$

Fig. 9 illustrates the key components of this algorithm, showing the mesh elements in red, curves in blue, and the process of angle assignment. The figure depicts how the tangent vector $\vec{T}$ is calculated at the point $\mathbf{p}^*$ on curve $\mathbf{c}_j$, which is the nearest point to the element's center $\mathbf{p}_i$. The distance d represents the shortest distance between $\mathbf{p}_i$ and $\mathbf{c}_j$. The figure also shows how the tangent vector $\vec{T}$ is used to determine the orientation angle θ_i.

The sequence of operations described above for mapping VAT orientations to finite elements is formally summarized in Algorithm 1, which details the routine for processing each element and populating the drape table.

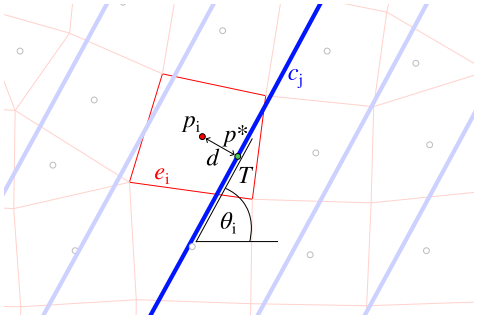

Fig. 9. VAT ply orientation mapping algorithm. Key elements include the finite element $\mathbf{e}_i$ (red outline) with its centroid $\mathbf{p}_i$ (red dot), the closest fiber path segment $\mathbf{c}_j$ (bold blue line), the closest point $\mathbf{p}^*$ (green dot) on $\mathbf{c}_j$ to $\mathbf{p}_i$, the tangent vector $\vec{T}$ at $\mathbf{p}^*$, the minimum distance d, and the resulting orientation angle θ_i for $\mathbf{e}_i$. Other FE mesh lines are shown in light red, and other fiber paths as light blue lines.

Algorithm 1 Mapping VAT orientations to finite elements and populating the drape table

for each finite element $\mathbf{e}_i$ **do**
  $p_i \leftarrow$ CENTROID($\mathbf{e}_i$)
  $(c_{j^*}, t^*) \leftarrow$ CLOSESTPOINT(p_i, C)
  $p_i^* \leftarrow c_{j^*}(t^*)$
  $\mathbf{T}_i \leftarrow$ tangent vector to c_{j^*} at parameter t^*
  $\theta_i \leftarrow$ ATAN2($T_{y,i}$, $T_{x,i}$)
  WRITE θ_i into the drape-table of the `.fem` file
end for

This discretization of the continuous curve data into element-specific angular values is crucial for maintaining the geometric integrity of the VAT design while enabling Finite Element Analysis (FEA). The resulting list of mapped angles to Finite Elements (FEs) provides a robust foundation for subsequent structural analyses and optimization processes in VAT composite design. This method bridges the gap between the continuous nature of AFP tow paths and the discrete representation required for finite element modeling, facilitating accurate simulation and analysis of VAT composite structures.

2.4. Implementation

The overall workflow was developed using Rhinoceros 3D (Rhino, version 8.16) including its integrated Grasshopper visual programming environment. The first optimizer (Optimizer I), a custom Python-based toolbox, was implemented in Python (version 3.12.4), while

Altair OptiStruct (version 2024.2) was utilized for the second optimizer (Optimizer II) to perform gradient-based thickness optimization.

This toolbox utilizes several key libraries: `NumPy` (version 1.26.4) for numerical operations, `SciPy` (version 1.13.0) for selected optimization routines, and notably `RBFOpt` (version 4.2.6) for the black-box spline optimization central to this work. Inter-process communication between the Python toolbox, Grasshopper workers, and the data-logging backend is handled via WebSockets (using the `websockets` library (version 12.0)).

Experiment metadata and results are stored in SQLite (accessed asynchronously via `aiosqlite` (version 0.20.0)), and all configuration files for the optimizer were managed using YAML, parsed with PyYAML (version 6.0.1). The workflow begins by importing model geometry into the `HyperWorks` (version 2023) FE software for simulation setup. This setup includes mesh creation and definition of forces, layer orientations, design variables, and material types. It also predefines the tow thickness which later on prompts the second optimizer, Optistruct, to discrete iteration steps in which thicknesses are integer multiples of the predefined tow thickness. The setup uses a drape table as a value container for the fiber directions at each element of the mesh, originally designed to simulate material deformation. An .fem file is generated, containing details like node positions, element descriptions for mesh creation, material properties, boundary conditions, applied forces, and optimization settings. This file also contains the drape table to assign fiber orientations, allowing unique orientations for each element and enabling FE simulations of curved paths. A Python-implemented parser reads the .fem file into Grasshopper, recreating the mesh and deriving a continuous geometry. An initial NURBS curve is generated on projection of the geometry in the XY-plane and then projected onto the 3D surface. Manufacturability checks ensure only feasible designs are produced. The spline is replicated across the entire surface, maintaining constant gaps without overlapping. To ensure complete surface coverage, the geometry is enlarged for replication, and the resulting paths are trimmed to the original surface. As the FEA environment requires discrete values, fiber angles are mapped to elements closest to the curve. The workflow is automated and parametric, allowing for easy adaptation to various components. The drape table is updated based on the current values of the mapping, and a new .fem file is created for use by the Optimizer II, ensuring that the latest design changes are incorporated into the FE environment. The study also incorporates a database with experimental metadata and a graphical user interface, enhancing the workflow's usability and data management capabilities. Fig. 3(b) schematically illustrates the configuration of a symmetric VAT laminate resulting from the optimization workflow, while (a) shows a standard laminate. Fig. 10 illustrates a simplified overview of the fully automated design generation and optimization workflow, structured into the three environments FEA, design, and manufacturing. The diagram is color-coded to highlight the core workflow segments: design generation (orange), manufacturability (green), and optimization (blue).

Nested loop optimization process for VAT laminate designs. To solve the optimization problem of VAT laminated composite structures, various optimization methods have been presented in recent years. Generally, these methods can be categorized into gradient-based methods, heuristic methods, metaheuristic methods, and hybrid methods [11].

In this approach, an automated design generation workflow utilizes a nested loop optimization process to produce a VAT laminate with a minimized mass. The type of optimizer was chosen based on the scope of the problem at the corresponding level. The first optimizer in this workflow is a metaheuristic-based optimizer, able to handle black-box problems. It adjusts the control points governing the reference curve of the VAT layer. The second optimizer (Optimizer II) is a gradient-based optimizer suitable for problems where the objective function is differentiable, which adjusts the thicknesses of the five individual layers in the laminate: t_{-45}, t_{45}, t_{90}, t_0, and t_{VAT}. The thicknesses are adjusted according to the load distribution effectiveness of the applied VAT layer design. If the VAT layer design improves load distribution and reduces structural weight, the second optimizer increases the thickness of this layer while reducing the thickness of other layers. If the VAT layer design is less effective or does not effectively distribute the load, the second optimizer uses a thinner layer and incorporates more standard ply designs. If the VAT layer does not contribute to the load distribution, the optimizer will exclude it, resulting in a laminate composed solely of standard orientation layers with optimized thicknesses. Both optimizers use mass as the objective function. As such, the first optimizer can map the effectiveness of a suggested curve based on the returned mass from the second optimizer.

This nested strategy was deliberately chosen due to critical interdependencies between the design tasks. Specifically, the effectiveness of a particular fiber path geometry, determined by the outer loop (Optimizer I), cannot be assessed in isolation, as any change in the fiber path directly influences the internal load distribution within the laminate, thus necessitating a corresponding re-evaluation of optimal layer thicknesses. Consequently, for each new fiber path proposed by Optimizer I, the ply thicknesses must be re-optimized by the inner loop (Optimizer II) to ensure that the minimum possible mass for that specific path configuration is achieved while satisfying all structural constraints, such as displacement limits. Crucially, the resulting minimized mass from Optimizer II serves as the objective function value that Optimizer I uses to evaluate the quality of its chosen fiber path. Without this inner loop re-optimizing thicknesses for each path, Optimizer I would assess fiber path variations against a static thickness distribution for all ply groups. This would mean the objective function (total mass) would remain constant, offering Optimizer I no basis to distinguish between different VAT designs and preventing an effective search for a optimized laminate.

Optimizer I: Black-box spline optimization. A Python-based optimization toolbox was developed to bridge the workflow steps of curve generation and the second optimizer with the spline optimization algorithms. The toolbox is centered around practical and intuitive execution and analysis of optimization runs, emphasizing both horizontal and vertical scalability, as illustrated in 11. For horizontal scalability, the toolbox is able to communicate locally or across the cloud with multiple workers running the curve generation and the first optimizer steps, enabling simultaneous or batch evaluations of design parameter sets. These workers can be deployed as multiple instances on the same machine or across several machines. To facilitate real-time communication and data exchange between the multiple workers and the optimization toolbox, WebSockets was chosen as the communication protocol. This choice was driven by the need for low-latency and persistent connections, which are critical for maintaining synchronization and efficiency in optimization runs. WebSockets enable seamless, bidirectional communication, allowing the toolbox to promptly send new design parameter sets and receive results from workers, whether they are operating locally or distributed across the cloud. This approach ensures that the toolbox is both robust and scalable. Vertical scalability is achieved through modularity that allows for streamlined integration of new optimization algorithms and an expanded or retracted design space. For instance, the toolbox can handle an increase in the number of unique VAT plies, and therefore the dimensionality, without source-code adaptation. Furthermore, the toolbox automatically logs all experiment data to a dedicated database for each experiment during an optimization. This is accomplished by monitoring the data traffic that passes through the server between the optimizer and the workers. The database is utilized not only for analyzing optimization runs but also as a cost-saving measure, as it allows for the reuse of results from previously evaluated data points if they are found in the database.

The optimization toolbox, and therefore the chosen algorithm, regard the curve generation and the first optimizer steps as a black-box function, in that the toolbox is unaware of this function's internal

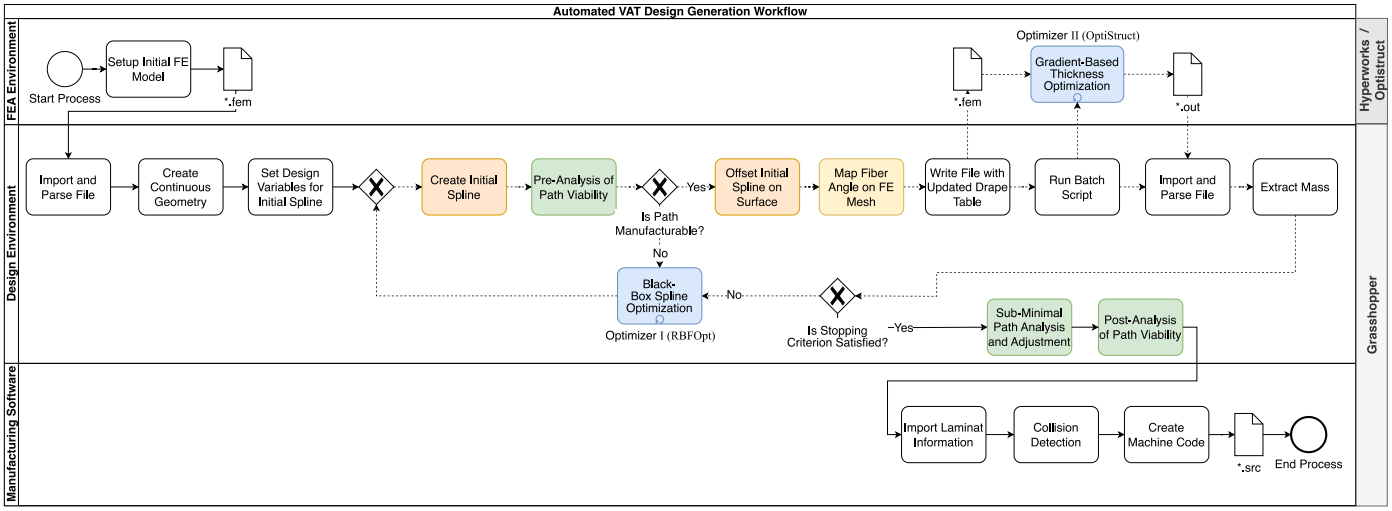

Fig. 10. Simplified overview of the automated design generation and optimization workflow for variable angle tow laminates. Color-coded highlights: design generation in orange, manufacturability in green, and optimization in blue.

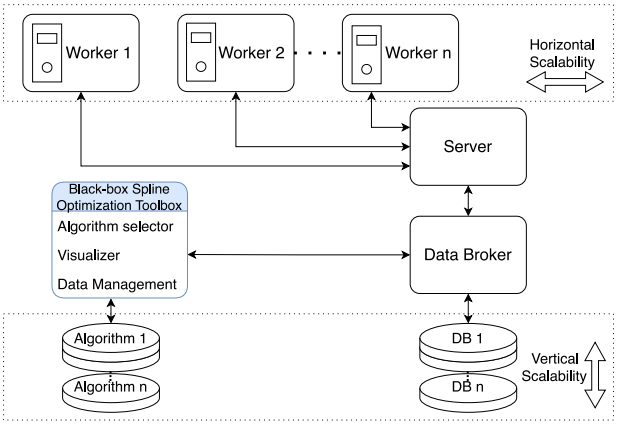

Fig. 11. Architecture of a scalable system for black-box spline optimization.

workings. The chosen algorithm's means of interaction with these steps, or the black-box function, is through sending one or more design parameter set x that belongs to the design parameter space X to the workers and receiving the corresponding total mass of the laminate m for each design parameter set.

The optimization problem solved by the outer-loop black-box optimizer (Optimizer I) aims to find the optimal set of NURBS spline parameters $\mathbf{x}$ that minimize the laminate mass returned by the inner-loop thickness optimization. The problem can be formulated as:

$$\min_{\mathbf{x}} m^*_{II}(\mathbf{x}) \quad \text{subject to:} \quad \begin{cases} \mathbf{x}^L \leq \mathbf{x} \leq \mathbf{x}^U \\ \mathbf{x} \in \mathbb{Z}^{N_x} \\ \text{PreAnalysis}(\mathbf{x}) = \text{pass} \end{cases} \tag{15}$$

where:

- $\mathbf{x} = (x_1, \ldots, x_{N_x})^T$ are the N_x integer design variables defining the NURBS reference curve, as detailed in Section 2.1.1. For the present work, $N_x = 4$.
- $m^*_{II}(\mathbf{x})$ is the objective function value, representing the optimized laminate mass achieved by the inner-loop optimizer (Optimizer II, see Eq. (16)) for the VAT ply design derived from $\mathbf{x}$.
- $\mathbf{x}^L$ and $\mathbf{x}^U$ are the lower and upper bounds for the design variables, respectively.
- The constraint PreAnalysis($\mathbf{x}$) = pass indicates that the VAT ply design derived from $\mathbf{x}$ successfully passes the pre-analysis checks described in Section 2.2. These checks primarily ensure that the reference curve and its projected offsets do not lead to local radii of curvature smaller than the minimum steering radius $r_{\text{min\_steering}}$ (defined in Table 1) and that no discontinuities are formed that would render the design unmanufacturable. If a design $\mathbf{x}$ fails these checks, $m^*_{II}(\mathbf{x})$ is assigned a penalty value, specifically the mass of an optimized standard laminate without any VAT layers. This effectively guides the search away from infeasible regions. The post-analysis (Section 2.2.2) and handling of sub-minimal paths (Section 2.2.3) are final checks and modifications rather than direct constraints within this optimization loop.

The design of a unique VAT ply is defined by four integer variables, x_1 through x_4, as described in Section 2.1. Using integers expands the range of applicable optimization algorithms, including those specific to discrete values. The parameter ranges are automatically adjusted to match component dimensions.

Given the optimizer's valid naivety of the inner workings of the curve generation and the first optimizer steps, the user must choose and appropriate second optimizers to incorporate in the toolbox. The first optimizer must be suitable to deal with the expensive, complex, non-linear, non-convex and discontinuous black-box function. The discontinuity is of special significance, since non-manufacturable designs represent a hyperplane that is the subset of data-points comprised of all non-manufacturable designs and the baseline mass of an optimized classical laminate not containing any VAT layers.

One suitable candidate is the free and open-source black-box optimizer Radial Basis Function Optimizer (RBFOpt) [57], which is a state-of-the-art model-based optimization library. It leverages a surrogate model that is continuously updated throughout an optimization run to approximate the underlying black-box function. The surrogate model is built using radial basis functions, a technique that is well-known in the field of machine learning. RBFOpt improves on its de facto predecessor algorithm [58] using several mechanics. Of note is the algorithm's better local performance. In the predecessor's work, the choice of the next point can be arbitrarily far from the currently known best point, which can severely hinder convergence. To alleviate this issue, RBFOpt adopts the strategy from [59] by progressively restricting the search area around the best known solution during a global search cycle. A further example of a significant improvement over the predecessor algorithm [58] is the automatic selection of the kernel function using a built-in cross-validation of several Radial Basis

$$\min_{\mathbf{t}} \text{Mass}(\mathbf{t}) = \rho \cdot A_{\text{surface}} \cdot \sum_{k=1}^{N_L} t_k \quad \text{subject to:} \quad \begin{cases} t_k \geq t_k^L & \text{for } k = 1, \ldots, N_L \\ t_k = N_k \cdot t_{\text{single\_ply}}, \quad N_k \in \mathbb{N}_0 & \text{for } k = 1, \ldots, N_L \\ u_j(\mathbf{t}) \leq u_{j,\text{allowable}} & \text{for critical DOFs } j = 1, \ldots, N_{\text{disp}} \end{cases} \tag{16}$$

Box I.

Function (RBF) models that were built using various kernel functions. Another useful feature of RBFOpt is the incorporation of a noisy oracle, which in essence is a supporting lower fidelity black-box function, to reduce computation time. In this work, the lower fidelity black-box is supporting curve generation and the first optimizer steps utilizing an FE model with a lower resolution mesh. The horizontal modularity of the optimization toolbox guarantees the integration of this feature, as the noisy oracle is essentially a second worker.

Optimizer II: Gradient-based thickness optimization. Upon completion of the previous steps, which involve generating splines based on the reference curve defined by the design variables set **x** recommended by the first optimizer, and mapping the angles of the splines at the finite element positions to their respective elements, the resulting values are recorded in the drape table. A new .fem file with this updated drape table is then generated and automatically utilized by the second optimizer.

The second optimizer in this study is the gradient-based optimizer implemented in OptiStruct. OptiStruct is a widely-used optimization tool that provides advanced structural analysis under static and dynamic loads. In this work, the thicknesses of the four standard ply orientations −45°, 0°, +45°, 90° along with the thickness of the additional VAT ply are considered as design variables. As such, the thicknesses of these five individual layers t_{-45}, t_{45}, t_{90}, t_0, and t_{VAT}, see Fig. 3, are optimized. Following the previously discussed aviation design principles, the laminate is configured symmetrically as $[\pm 45/90/0/VAT]_s$, with the VAT layer centrally positioned (Fig. 3. This arrangement, including the protective ±45° outer plies, adheres to industry standards while potentially enhancing the laminate's structural performance. The optimization process aims to determine the optimal thickness for each layer within this configuration.

The inner-loop optimization problem, solved by the gradient-based optimizer OptiStruct (Optimizer II), seeks to minimize the laminate mass for a given VAT ply orientation (defined by Optimizer I by **x**) by adjusting the thicknesses of individual ply groups. The formulation is (see the Eq. (16) in Box I): where:

- $\mathbf{t} = (t_1, \ldots, t_{N_L})^T$ is the vector of thicknesses for the N_L distinct ply orientation groups (e.g., $t_{-45}, t_{45}, t_{90}, t_0, t_{VAT}$). For the present work, $N_L = 5$.
- Mass(**t**) is the total mass of the laminate, with ρ being the material density (Table 2) and A_{surface} the component's surface area.
- t_k^L are the prescribed lower bounds for ply thicknesses. This can be $1 \cdot t_{\text{single\_ply}}$ (where $t_{\text{single\_ply}}$ is the tow thickness from Table 1) to ensure presence, or can be coupled for the 10% thickness rule per orientation, as discussed in Section 3.
- The constraint $t_k = N_k \cdot t_{\text{single\_ply}}$ enforces that thicknesses are integer multiples of a single ply's thickness $t_{\text{single\_ply}}$. While OptiStruct may work with continuous variables, the final design adheres to this discrete sizing constraint.
- $u_j(\mathbf{t})$ are the displacements at N_{disp} critical degrees of freedom (DOFs), which must not exceed their allowable values $u_{j,\text{allowable}}$.

3. Numerical results and discussion

The methodology outlined in this paper was applied to two distinct examples: a simple 2D plate, used as an academic example, and a representative 3D geometry inspired by a section of a wing shell from a commercial aircraft. The primary focus of the optimization process discussed in this paper was to develop a design that minimizes weight while ensuring structural integrity under all specified loads and meeting the defined stiffness requirements. The component, load case, and constraints selection was exemplarily chosen to demonstrate the applicability of the methodology. It should be noted that the efficacy of the optimal laminate design and the extent of weight reduction relative to standard laminates significantly depend on the capabilities of the manufacturing machine, the characteristics of the component, and the specifics of the load scenario. The optimization incorporated nine variables, comprising five variables corresponding to the thicknesses of individual layers $(t_{-45}, t_{45}, t_{90}, t_0, t_{VAT})$ as integer multiples of the tow thickness, and four variables that defined the shape of the NURBS spline (x_1, x_2, x_3, x_4).

Table 1
Design Parameters for Optimization.

Parameter	Unit	Value
Tow width	mm	6.35
Tow thickness	mm	0.184
Tow gap	mm	0.5
Minimum steering radius	mm	70
Minimum cutting length	mm	45

Table 2
Assumed material properties of the CFRP IMA-M21.

Property	Unit	Value
Fiber direction Young's modulus E_{11}	GPa	178.0
Transverse direction Young's modulus E_{22}	GPa	9.5
Shear modulus G_{12}	GPa	5.2
Shear modulus G_{23}	GPa	2.5
Poisson's ratio ν_{12}	–	0.3
Theoretical calculated laminate density ρ	g/cm^3	1.58

For both the 2D plate and 3D wing shell case studies, these four NURBS variables were used to define the initial reference spline according to the construction method detailed in Section 2.1.1

For the optimization process, representative values from Table 1 were utilized. Specifically, tow width and tow thickness describe the dimensions of the prepreg material employed, and tow gap indicates the uniform spacing between the tows. Furthermore, both the standard orientation layers and the VAT layers were designed as full plies and cover the entire surface.

The CFRP material chosen for all calculations, of both the baseline and the VAT variants of the laminates, is Hexcel's HexPly M21 prepreg reinforced with HexTow IMA carbon fiber. This selection was made due to the extensive public availability of M21 data and its similarity to HexPly M21E, which is employed in significant aerospace applications such as the A350 XWB, ensuring compatibility and relevance in aerospace research contexts. An excerpt from the relevant material properties is provided in Table 2.

The black-box spline optimization in both examples employed the RBFOpt algorithm as Optimizer I with RBFOpt v4.2.6. This state-of-the-art, model-based optimization method was chosen for its ability to handle complex, non-linear design spaces efficiently. Table 3 lists the RBFOpt parameters employed for Optimizer I in this work. The

Table 3
Set of RBFOpt parameters used in this work for the black-box Optimizer (Optimizer I). Status 'user' = value chosen for this study, 'default' = unchanged RBFOpt v4.2.6 factory value.

Parameter	Unit	Value	Status
Design-space dimension (n)	–	4	User
Algorithm (`algorithm`)	–	`MSRSM`	Default
Radial basis function (`rbf`)	–	`auto`	Default
RBF shape parameter (`rbf_shape_parameter`)	–	0.1	Default
Initialization strategy (`init_strategy`)	–	Latin-hypercube (maximin)	Default
Initial-sample fraction (`init_sample_fraction`)	–	10/20[a] (plate/wing)	User
Include midpoint in start set (`init_include_midpoint`)	–	True	Default
Tolerance for acceptable improvement (`eps_impr`)	kg	0.001	User
Optimality tolerance (`eps_opt`)	–	0.01	Default
Numerical zero threshold (`eps_zero`)	–	1×10^{-15}	Default
Maximum evaluations (`max_evaluations`)	–	2000/3000 (plate/wing)	User
Maximum iterations (`max_iterations`)	–	2100/3100 (plate/wing)	User
Discarded window size (`discarded_window_size`)	–	30	Default
Max. fraction discarded (`max_fraction_discarded`)	–	0.5	Default
Global search method	–	`genetic`	Default
Global search points per cycle (`num_global_searches`)	–	5	Default
GA base population size	–	400	Default
GA number of generations	–	20	Default
Number of CPUs (`num_cpus`)	–	1	Default

[a] The initial-sample fraction of 20 generates $(n+1) \times 20 = 100$ Latin-hypercube points for $n = 4$.

Table 4
Set of OptiStruct parameters used in this work for the ply-thickness optimizer (Optimizer II). Status 'user' = value chosen for this study, 'default' = unchanged OptiStruct 2024.2 factory value. A discrete step of 0.125 mm enforces integer multiples of the tow thickness t_{tow}.

Parameter	Unit	Value	Status
Algorithm (`METHOD`)	–	`MFD`	Default
Iteration limit (`MAXITER`)	–	30	Default
Move limit per iteration (`DELTOPT`)	%	±20	Default
Objective tolerance (`ROBJTOL`)	–	0.01	Default
Constraint tolerance (`RCTLTOL`)	–	0.01	Default
Sensitivities (`SENSREL`)	–	Analytical	Default
Discrete sizing activated (`DISCRETE`)	–	`ON`	User
Thickness increment (`STEP`)	mm	0.125[a]	User

[a] In HyperMesh's internal unit of 0.01 mm this corresponds to `STEP = 12.5`.

'Status' column for each parameter indicates whether the value was user-defined for this study or if it corresponds to an unchanged factory default.

For the gradient-based thickness optimization in both examples, Altair's OptiStruct, a module within the HyperWorks suite, was employed as Optimizer II. This structural analysis and optimization software was selected for its robust capabilities in handling composite structures and its efficient gradient-based algorithms.

The ply-thickness optimization is carried out with *Altair* OptiStruct 2024.2. OptiStruct defaults to its gradient-based *Method of Feasible Directions* (MFD) sequential approximation scheme. Table 4 lists all optimizer parameters, classified as either unchanged factory defaults or values chosen by the authors (status *user*).

To provide a comprehensive overview of the optimization formulations employed in both case studies, Table 5 summarizes the common elements and case-specific parameters for both the academic 2D plate example and the wing shell application. This formulation summary facilitates comparison between the cases and ensures reproducibility of the methodology.

Table 5
Summary of optimization formulation for both case studies.

Element	Academic example (2D)	Wing shell (3D)
Objective function and design variables		
Objective function	Minimize total laminate mass	
Design variables	Optimizer I: x_1, x_2, x_3, x_4 (NURBS control points) Optimizer II: $t_{-45}, t_{45}, t_{90}, t_0, t_{VAT}$ (layer thicknesses)	
Manufacturing constraints		
	• Minimum curvature radius r_{min} • Pre-analysis path viability checks • No gaps/overlaps • Integer multiples of single-ply thickness	
Variable bounds		
	$x_L \le x \le x_U$ (component-adapted) $t_k \ge t_k^L$ (minimum thickness) $t_k = N_k \times t_{single-ply},\ N_k \in \mathbb{N}_0$	
Finite element modeling		
Element type	Shell elements (first-order)	
Case-specific parameters		
Structural constraints	Max displacement ≤1 mm at load points	Max displacement ≤5 mm at measurement points
Applied loads	5 × 4000 N	33 × 1000 N
Load direction	[1, 1, 0.1]	[0, −1, 0]
Boundary conditions	Fixed lower edge	Fixed wing root
Component dimensions	210 mm × 297 mm (A4 size)	1170 mm × 788 mm (Scaled wing section)
Mesh details	266 elements	4662 elements

3.1. Academic example: Rectangular 2D plate

For this academic example, a rectangular 2D plate with dimensions matching those of an A4 sheet (210 mm × 297 mm) was utilized. The 0° fiber direction was defined to be parallel to the longer edge of the rectangle, corresponding to the vector $\begin{pmatrix} 0 & 1 & 0 \end{pmatrix}$ in the global coordinate system. Fig. 12 illustrates the mesh consisting of 266 CQUAD4 (4-node quadrilateral) first order shell elements, the applied boundary conditions, and the forces acting on the plate. The load case and boundary conditions were chosen exemplarily to apply the method to a relatively simple case, thereby demonstrating its applicability. In this study, the plate was subjected to five loads of 4000 N each, applied in the direction of the vector $\begin{pmatrix} 1 & 1 & 0.1 \end{pmatrix}$, while the lower edge was fixed. Five total displacement measurement points were placed at the points of contact of the forces. These total displacement measurements were used as constraints for the gradient-based thickness optimizer

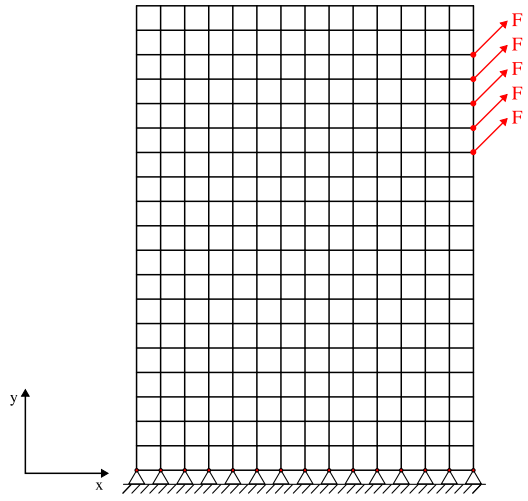

Fig. 12. FE mesh representation of a rectangular 2D plate, consisting of 266 first-order shell elements, with applied forces and boundary conditions. The illustration shows the discretized domain, external loads acting on the plate, and the fixed constraint along the bottom edge.

Table 6
Combined load application and displacement measurement specifications for the 2D plate.

Point No.	Node ID	X (mm)	Y (mm)
1	240	210.0	198.421
2	239	210.0	213.684
3	238	210.0	228.947
4	237	210.0	244.211
5	236	210.0	259.473

Applied load: 4000 N per point in direction (1, 1, 0.1).
Maximum displacement constraint: 1.0 mm per point

Optistruct (Optimizer II). The maximum allowable displacement for all nodes was set to 1 mm.

To ensure complete reproducibility of the 2D plate analysis, Table 6 provides the exact nodal coordinates for all five load application and displacement measurement points.

Fig. 13 illustrates the curves generated by the automated design optimization workflow. The left side of the figure shows the initial NURBS curve in blue, along with its derived offset curves in black. These curves represent the centerlines of the tows in the AFP process. The right side of the figure demonstrates the discrete mapping of these continuous curves onto individual FEs, as described in Section 2.3, highlighting the transition from the continuous design space to the discrete FE representation.

The termination condition for the optimization of the academic example was set to 2000 evaluations, as depicted in Fig. 14, which illustrates the complete optimization process. Fig. 15 illustrates a representative sample ranging from 1000 to 1650 evaluations. This excerpt highlights distinct phases in the optimization search, visually demarcated by dashed lines, which indicate points where Optimizer I (RBFOpt) significantly adjusted its internal search strategy due to detected stagnation. Each point represents the mass at a given iteration and corresponds to a design, with the global minimum mass of the explored design space highlighted in red. This visualization demonstrates the effectiveness of the optimization process in reducing the overall structural weight. While the plot primarily shows the evolution of mass, compliance with imposed constraints is ensured through the optimization criteria set prior to and during the evaluation process.

The black-box spline optimizer RBFOpt (Optimizer I) begins with an initial exploration phase using Latin Hypercube Sampling. Subsequently, it iteratively refines its surrogate model and explores the

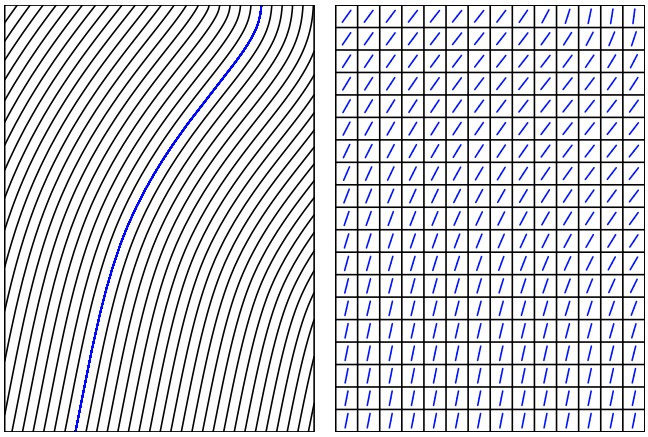

Fig. 13. Schematic representation of an optimized VAT ply configuration. The left panel depicts the curvilinear center lines of AFP fiber paths. The right panel illustrates the corresponding fiber orientation angles mapped onto discrete FEs.

design space. Stagnation, which prompts a significant adjustment in search strategy (indicated as a "restart" in Fig. 15), is detected by RBFOpt whenever the best known solution does not improve by at least the specified threshold for acceptable improvement, `eps_impr` = 0.001 kg (as defined in Table 3). The decision to adjust the search strategy due to stagnation is governed by RBFOpt's default internal parameters. For instance, if, within a rolling window of evaluations (controlled by `discarded_window_size`, default: 30 evaluations, see Table 3), a high proportion of candidate points (determined by `max_fraction_discarded`, default: 0.5, see Table 3) are deemed unpromising or fail to yield an improvement greater than `eps_impr`, RBFOpt alters its search strategy. This internal "restart" of the search strategy might involve intensifying exploration in different regions of the design space or making substantial changes to its surrogate model. Such strategy shifts can sometimes lead to the evaluation of points resembling an initial exploration phase or a temporary increase in the objective function value if non-manufacturable designs are encountered (appearing as a "plateau" following a "restart" line in Fig. 15). Depending on the regions explored after such a strategy adjustment, the subsequent convergence to a local minimum can vary. Thus, each phase demarcated by a "restart" line in Fig. 15 can be interpreted as comprising a period of renewed or altered exploration by RBFOpt in response to detected stagnation, followed by a convergence phase, and potentially further periods of stagnation leading to subsequent strategy adjustments.

In such cases of non-manufacturable fiber paths, the baseline mass of a classical laminate design is returned to Optimizer I. This mechanism, where infeasible designs are quickly identified and penalized without triggering computationally intensive OptiStruct runs (Optimizer II), significantly enhances computational efficiency. Of the 2000 design evaluations performed, 1520 were identified as infeasible by Optimizer I early in the process, thus avoiding unnecessary calls to Optimizer II and allowing the optimization to efficiently navigate the design space.

The resulting mass of the VAT part generated by the automated design optimization procedure was benchmarked against the baseline mass of the optimized classical laminate that only utilizes the four standard ply orientations of −45°, 0°, +45°, and 90°. The baseline mass is 1.65683 kg, whilst the mass of the VAT optimized part is 1.53353 kg, yielding a 7.44% reduction in mass. Table 7 presents the optimized design configuration, detailing the number of plies and the thickness of each layer. Each layer's thickness is an integer multiple of the thickness of the CFRP tow, adhering to the manufacturability constraint that the AFP system can only lay down one complete tow thickness at a time. The data demonstrates that the VAT ply was heavily

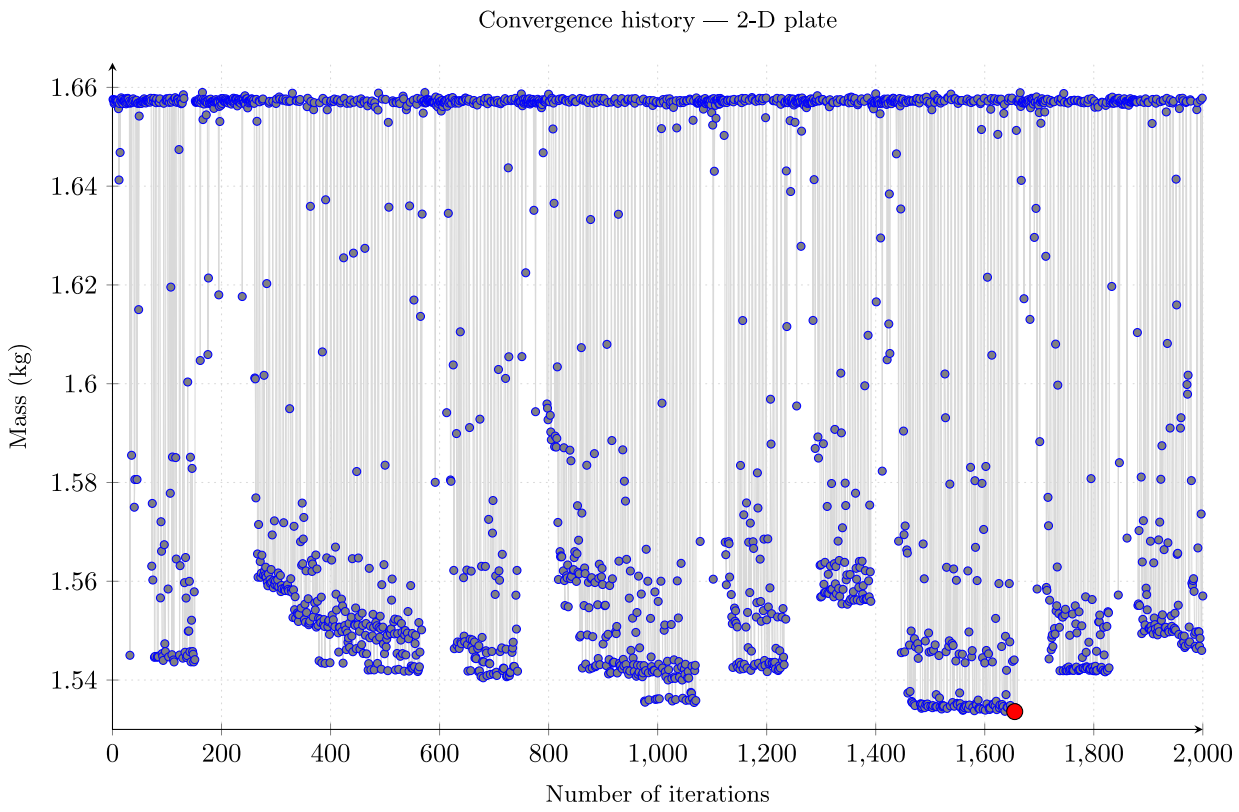

Fig. 14. Convergence history of the 2-D plate optimization (0–2000 iterations). Mass is plotted for every iteration; the global minimum is marked in red.

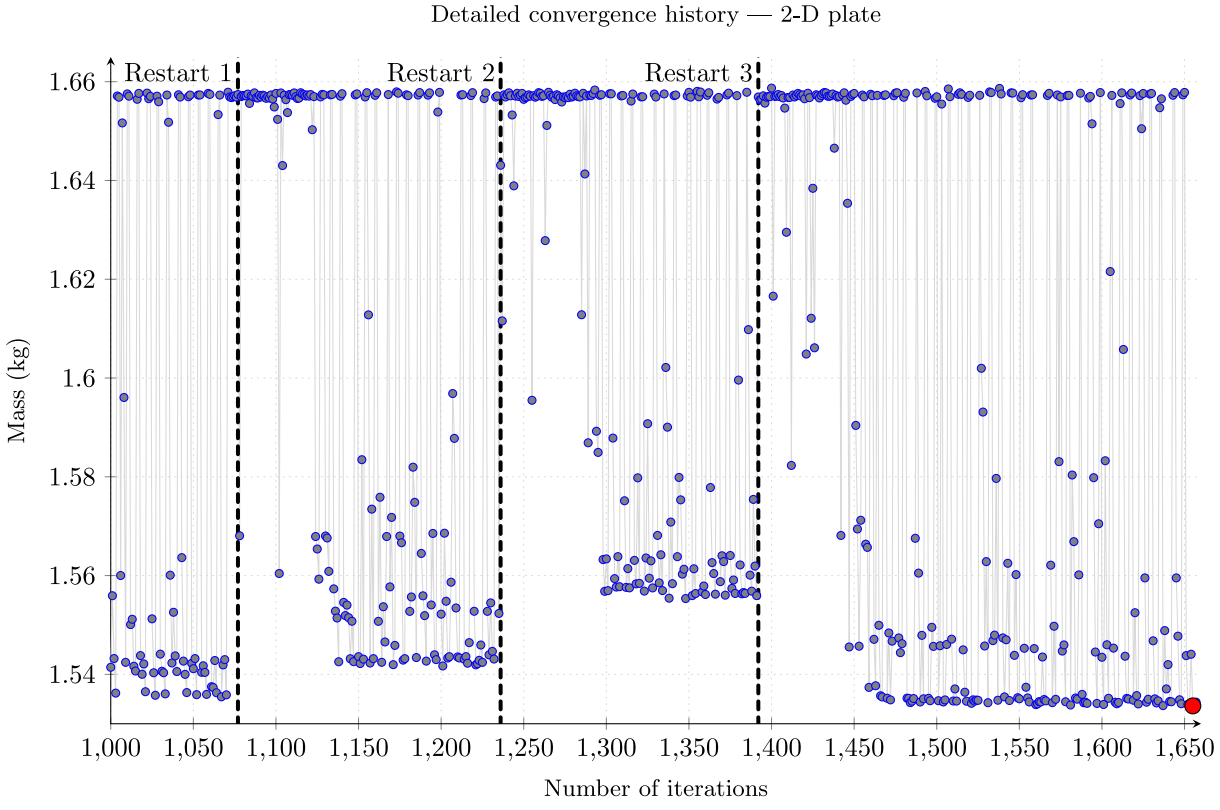

Fig. 15. Detailed convergence history of the 2-D plate optimization (iterations 1000–1650). Mass is plotted for every iteration; This excerpt focuses on the range where significant changes occur, with the global minimum highlighted in red.

Table 7
Comparison of optimized classical and VAT laminates for the rectangular 2D plate, under the condition that at least one ply is present for each orientation.

	Thickness (mm)					No. of Plies					Mass (kg)
	t_{-45}	t_{45}	t_{90}	t_0	t_{VAT}	p_{-45}	p_{45}	p_{90}	p_0	p_{VAT}	m
Classical laminate	5.152	0.184	0.184	3.128	–	28	1	1	17	–	1.65683
Optimized VAT laminate	0.184	0.184	0.184	0.184	7.176	1	1	1	1	39	1.53353

Table 8
Comparison of optimized classical and VAT laminates for the rectangular 2D plate, with a design restriction requiring a minimum of 10% of the total thickness per orientation.

	Thickness (mm)					No. of Plies					Mass (kg)
	t_{-45}	t_{45}	t_{90}	t_0	t_{VAT}	p_{-45}	p_{45}	p_{90}	p_0	p_{VAT}	m
Classical laminate	4.968	0.920	0.920	2.392	–	27	5	5	13	–	1.77048
Optimized VAT laminate	0.920	0.920	0.920	1.840	4.416	5	5	5	10	24	1.73508

favored by Optimizer II and occupies 91% of the total thickness of the laminate. Meanwhile, each of the standard orientation plies −45°, 0°, +45°, and 90° was incorporated as a single layer. The reason for this incorporation is the restriction imposed on Optimizer II to use at least a single layer per orientation. The requirement of including at least one layer of each standard orientation was imposed to ensure a more realistic and robust laminate design. This approach acknowledges that in practical applications, laminates are rarely optimized for a single load case but must withstand various, often unpredicted, loading scenarios. By maintaining a minimum presence of each orientation, the laminate retains a degree of multi-directional strength and stiffness, which is crucial for overall structural integrity and damage tolerance. This design principle aligns with industry practices where purely unidirectional or overly specialized laminates are generally avoided due to their potential vulnerability to off-axis loads.

The optimization was subsequently conducted with an additional design constraint requiring a minimum of 10% of the total thickness for each orientation, adhering to a well-established guideline in the aerospace industry. Under this constraint, the mass reduction decreased significantly to 2%. This diminished optimization potential can be primarily attributed to the fact that the guideline from which this restriction originates was developed without consideration for VAT plies resulting in laminate configurations that are suboptimal for configurations including VAT plies. The 10% rule inherently limits the design freedom, forcing the inclusion of standard orientation plies that might otherwise be reduced or eliminated in favor of the more efficient VAT ply. This constraint, while ensuring a more balanced ply distribution, inherently restricts the weight reduction potential of the VAT configuration. Table 8 presents the optimized design configuration under these constraints, detailing the number of plies and the thickness of each layer. The results highlight the trade-off between adhering to traditional design guidelines and exploiting the full potential of advanced composite configurations like VAT laminates.

3.2. Wing shell: Double-curved 3D shape

The next design example presents a more realistic and large-scale application with increased complexity, and of direct relevance to the aerospace industry. The component under consideration is a representative model of a cropped and scaled-down lower wing shell of a commercial aircraft. This component exhibits a double-curved 3D geometry and incorporates discontinuities in the form of manholes, which are utilized for wing maintenance and servicing. A section of the original wing was selected and scaled down by a factor of 50 to reduce computational time requirements. The resulting component has a longest edge of 1170 mm and an edge mounted to the aircraft measuring 788 mm. The 0° fiber direction was defined to be parallel to the longest edge of the component, corresponding to the vector $(0.46 \quad 0.89 \quad 0.05)$ in the global coordinate system. The mesh is comprised of 4662 elements, including 165 CTRIA3 (3-node triangular) and 4497 CQUAD4 (4-node quadrilateral) elements, which are common first order shell element types in FEA, with activated membrane and bending properties as depicted in Fig. 16. This level of mesh complexity significantly influences the computation time required for optimization compared to the previous academic example. In this study, the scaled wing shell was subjected to 33 loads, each exerting 1000 N, distributed along a line of nodes parallel to the wing root and acting in the direction of the negative y-axis, corresponding to the vector $(0 \quad -1 \quad 0)$. For clarity, Fig. 16 depicts a single representative force vector, symbolizing the direction of all applied forces. The individual points of force application are not explicitly shown in the figure for visual simplicity. The exact nodal coordinates of these load application points are available upon request to facilitate complete reproducibility of the analysis. The wing root was fixed, representing the interface between the wing and the aircraft fuselage. Seven total displacement measurement points were positioned at equidistant intervals along the line connecting the points of contact of the forces. These total displacement measurements served as constraints for the gradient-based thickness optimizer OptiStruct (Optimizer II). The total allowable displacement was set to 5 mm. It should be noted that the magnitude and distribution of the forces were chosen for demonstrative purposes only and do not reflect real-world loading conditions.

Table 9
Displacement measurement point specifications for the 3D wing shell.

Measurement No.	Node ID	X (mm)	Y (mm)	Z (mm)
1	3820	700	−847.12	−13.25
2	3864	700	−740.96	−28.22
3	3924	700	−604.488	−46.47
4	3999	700	−438.04	−66.42
5	4121	700	−220.55	−86.17
6	4195	700	−86.59	−95.08
7	4254	700	20.33	−100.42

Maximum displacement constraint: 5.0 mm per point.

Fig. 17 presents two views of an optimized VAT ply configuration for a wing section. The left panel shows the equidistant curvilinear center lines representing the AFP fiber paths across the wing surface. The right panel displays the same design with the fiber orientations mapped onto discrete FEs. This visualization demonstrates the translation of the continuous VAT design into a discrete format suitable for FEA.

To ensure reproducibility of the displacement constraint specifications, Table 9 provides the exact nodal coordinates of the seven displacement measurement points distributed across the wing shell structure.

The termination condition for the optimization of the academic example was set to 3000 evaluations, as depicted in Fig. 18, which illustrates the complete optimization process. Fig. 19 illustrates a representative sample ranging from 1500 to 2400 evaluations. Of the 3000 design iterations performed, 271 were deemed infeasible early in the

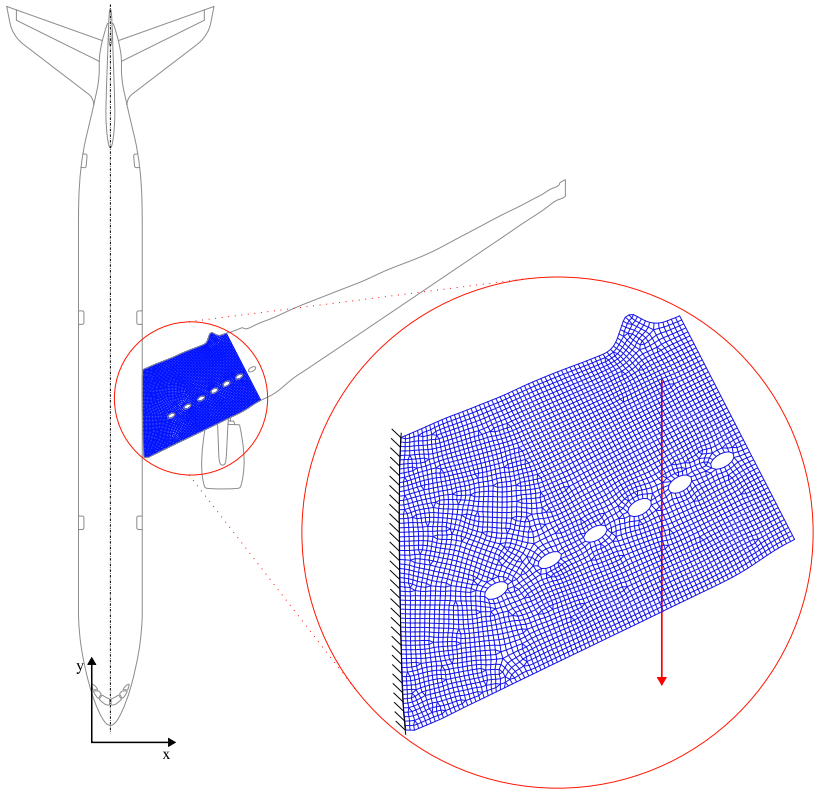

Fig. 16. Schematic representation of a commercial aircraft showing the selected section of the lower wing shell. The magnified view highlights the FE mesh of the selected section, which is comprised of 4662 first-order shell elements, its boundary conditions, and a force representative acting on it. The load is applied along a line parallel to the wing root at a distance of 700 mm.

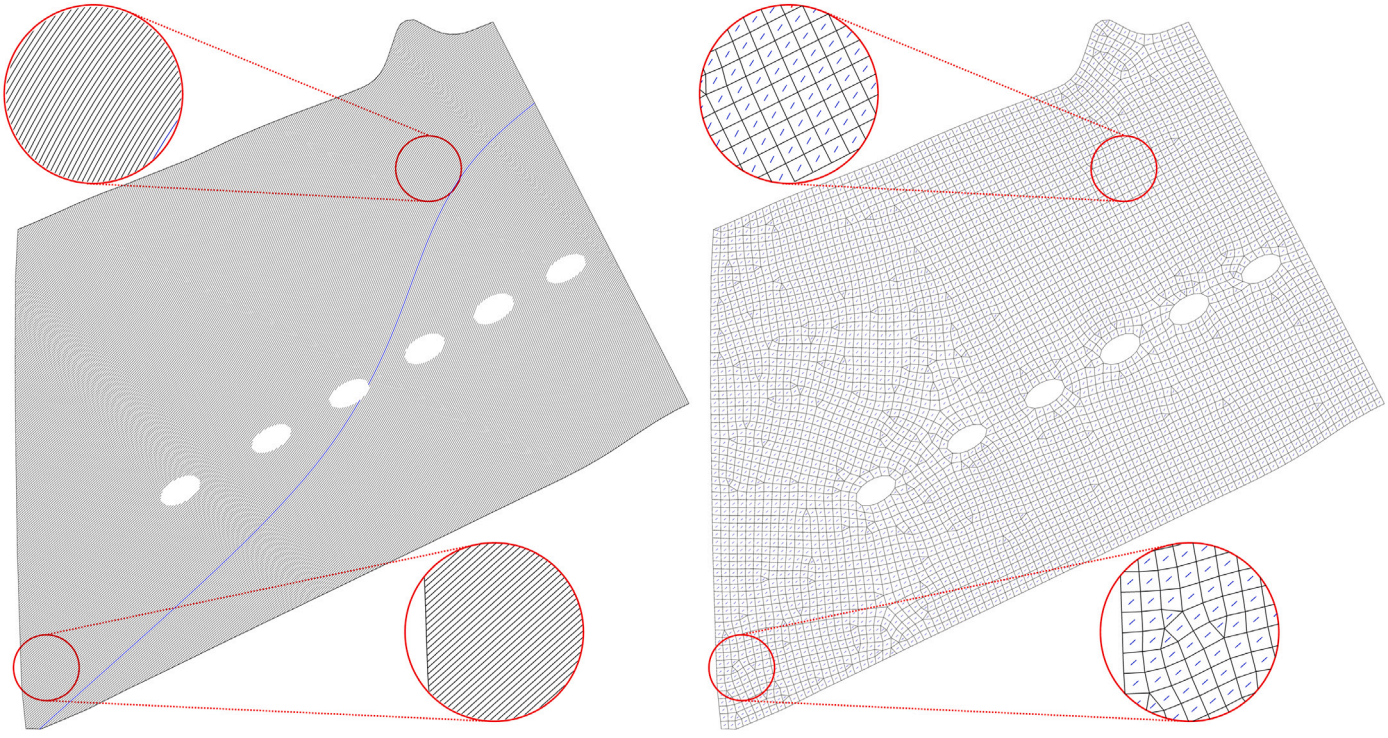

Fig. 17. Schematic representation of an optimized VAT ply configuration. The wing section to the left depicts the curvilinear center lines of AFP fiber paths. The wing section to the right illustrates the corresponding fiber orientation angles mapped onto discrete FEs.

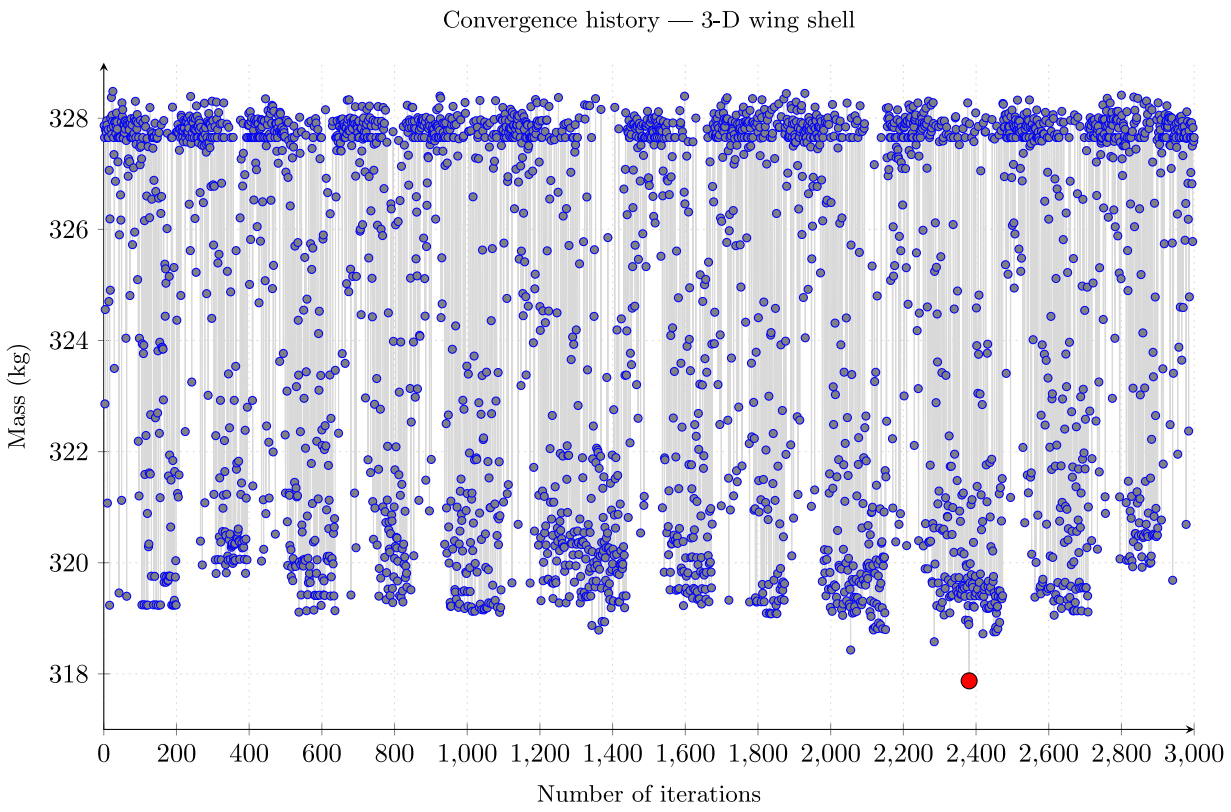

Fig. 18. Convergence history of the wing shell optimization (0–3000 iterations). Mass is plotted for every iteration; the global minimum is marked in red.

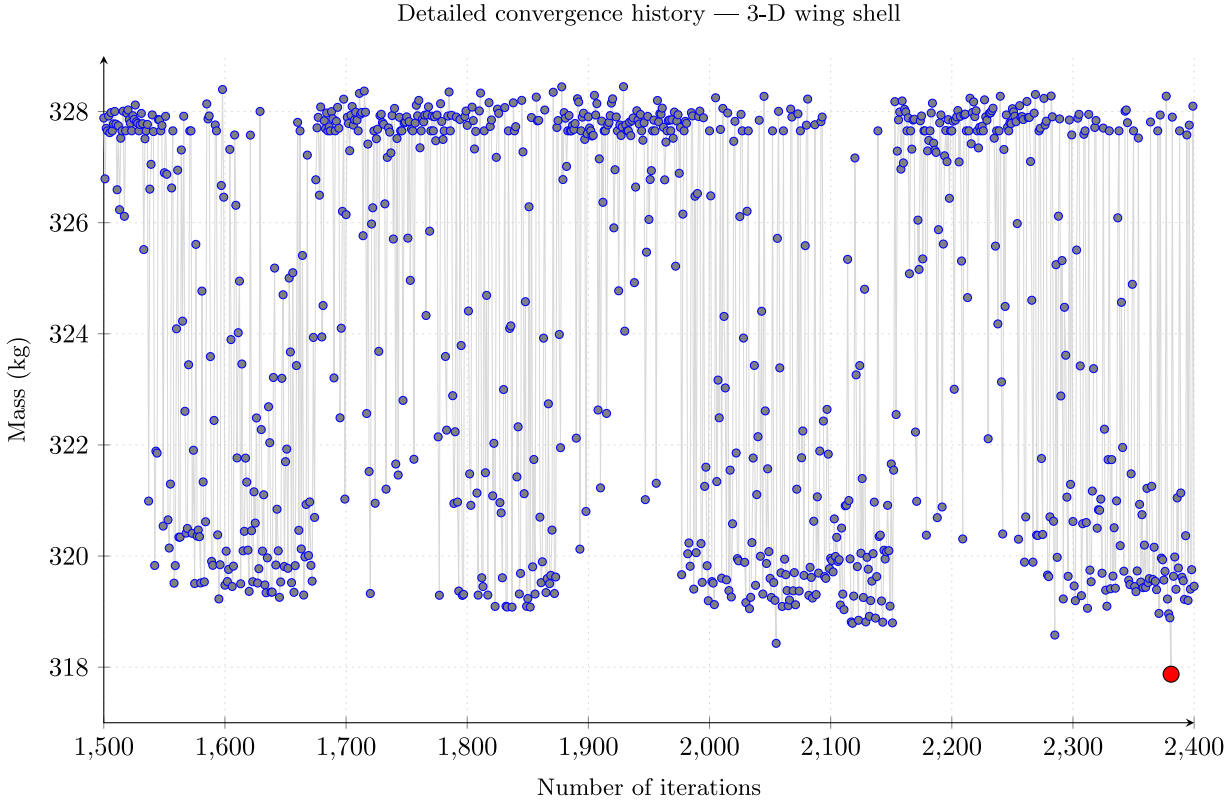

Fig. 19. Detailed convergence history of the wing shell optimization (iterations 1500–2400). Mass is plotted for every iteration; This excerpt focuses on the range where significant changes occur, with the global minimum highlighted in red.

Table 10
Comparison of optimized classical and VAT laminates for the Double-Curved 3D Shape, under the condition that at least one ply is present for each orientation.

	Thickness (mm)					No. of plies					Mass (kg)
	t_{-45}	t_{45}	t_{90}	t_0	t_{VAT}	p_{-45}	p_{45}	p_{90}	p_0	p_{VAT}	m
Classical laminate	1.84	7.912	1.104	13.064	–	10	43	6	71	–	327.653
Optimized VAT laminate	0.368	4.048	0.184	5.152	13.432	2	22	1	28	73	317.874

Table 11
Comparison of classical and optimized VAT laminates for the Double-Curved 3D Shape, with a design restriction requiring a minimum of 10% of the total thickness per orientation.

	Thickness (mm)					No. of plies					Mass (kg)
	t_{-45}	t_{45}	t_{90}	t_0	t_{VAT}	p_{-45}	p_{45}	p_{90}	p_0	p_{VAT}	m
Classical laminate	3.680	7.544	3.312	9.936	–	20	41	18	54	–	334.137
Optimized VAT laminate	2.392	5.888	2.392	7.360	5.888	13	32	13	40	32	326.600

process and thus did not trigger an inner iteration. No OptiStruct run was executed in these cases.

The resulting mass of the VAT laminate generated by the automated design optimization was benchmarked against the baseline mass of an optimized classical laminate that only utilizes the four standard ply orientations of −45°, 0°, +45°, and 90°. Under the condition that at least one ply is present for each orientation, the baseline mass is 327.653 kg, whilst the mass of the optimized VAT laminate is 317.874 kg, yielding a 3% reduction in mass. Table 10 presents the optimized design configuration detailing the thicknesses of the individual plies, the integer multiple of the tow thickness for each ply to achieve its respective manufacturable thickness, and the mass for both the classical laminate and the optimized VAT laminate. The results show that for the classical laminate, the thickness of the 0° ply occupies around 55% of the total laminate thickness, followed by the 45° ply at 33%. The thickness needed for these two plies was significantly reduced in the optimized VAT laminate, with the thickness of the 0° ply occupying only 22% of the total laminate thickness, and that of the 45° ply occupying 17%. The thickness of the VAT ply dominates at 58%. This showcases the significance of the VAT ply regarding achieving the desirable mechanical properties defined by the constraints of the experiment. The 90° ply was incorporated as a single layer, meeting the minimum requirement of one ply per orientation. In total, the optimized VAT laminate is composed of 126 layers whereas the traditional laminate requires 130 layers.

Analogous to the academic example, a second experiment was subsequently conducted with an additional design constraint requiring a minimum of 10% of the total thickness for each orientation. Under this constraint, the mass reduction decreased to 2.3% (see Table 11). In contrast to the academic example, the decrease in mass reduction is relatively small. The smaller impact of the 10% guideline on mass reduction in the larger wing shell example, compared to the academic plate example, can be primarily attributed to the initial distribution of ply orientations in the optimized design. In the wing shell case, the VAT plies did not dominate the laminate composition to the same extent as in the academic example. Instead, a more balanced distribution of standard orientations was already present, with other ply directions playing significant roles in carrying the loads of the 3D structure. This initial balance meant that the imposition of the 10% guideline did not force as dramatic a redistribution of ply thicknesses as it did in the academic example. Consequently, the optimized VAT design for the wing shell was inherently closer to meeting the 10% guideline, resulting in a less severe impact on the achievable mass reduction when this constraint was applied. This observation highlights the importance of considering the specific load cases and structural complexities when evaluating the potential benefits of VAT designs in different applications. Table 11 displays the optimized design configuration, detailing the number of plies and the thickness of each layer, resulting in 133 layers (classical) in contrast to 130 layers for the optimized laminate.

The results from both the academic example and the wing shell case study provide valuable insights into the potential and limitations of VAT laminate designs in different applications, particularly under relatively simple loading conditions. In the academic example of a 2D plate, the VAT design achieved a significant mass reduction of 7.44% compared to the classical laminate design when only constrained to include at least one ply of each orientation. Similarly, the more complex 3D wing shell example showed a 3% mass reduction with the minimal ply constraint, demonstrating that VAT designs can offer measurable benefits even when applied to more complex geometries under relatively straightforward loading conditions.

Crucially, this study has demonstrated the reliability and effectiveness of the automated design workflow in generating VAT laminate designs. The workflow consistently produced designs that not only led to mass reduction but also ensured manufacturability, a key consideration for practical implementation. The resulting designs are directly compatible with AFP machines, bridging the gap between theoretical optimization and practical manufacturing constraints. This achievement underscores the potential of the automated workflow to streamline the design-to-manufacturing process for VAT laminates in real-world applications.

It is important to emphasize that these mass reductions and manufacturable designs were achieved under load cases that were intentionally kept simple for demonstration purposes. The fact that VAT designs could provide substantial weight savings even in these basic scenarios, while maintaining manufacturability, suggests that their potential benefits could be even more pronounced in more complex, multi-load case situations typical of actual aerospace structures.

3.3. Computational resources

To provide insight into the computational efficiency and practicality of the proposed approach, this section details the hardware used and the computational times observed for the optimization runs. All optimizations presented in this study were performed on a laptop equipped with an Intel Core i7-1355U (13th Generation, 1.70 GHz) and 16 GB of RAM, running Windows 10 (64-bit). The nested optimization procedure consists of an outer iteration loop (referred to as “One Iteration (Outer Loop)”) that includes calls to the inner gradient-based optimization (referred to as “One Iteration (OptiStruct)”). Hence, “One Iteration (OptiStruct)” is fully contained within “One Iteration (Outer Loop).” Table 12 summarizes the average computation time per iteration for each of these loops, as well as the overall runtime for both the Academic Example and the representative Wing Shell, each analyzed with and without the 10% thickness constraint.

Total optimization runtimes for the 2D plate examples ranged from 2 h 19 min to 3 h 31 min (average outer loop iterations: 11–12 s). The more complex 3D wing shell examples required considerably longer total runtimes, extending from 1 day, 5 h, and 36 min to 1 day, 7 h, and 24 min (average outer loop iterations: 23–25 s).

Table 12
Computation times and hardware specifications. The column "One Iteration (Outer Loop)" refers to the average duration of a single full iteration of the nested optimization loop, "One Iteration (OptiStruct)" indicates the average duration of the gradient-based optimizer's iteration, and "total" represents the overall runtime from start to finish.

Study	One iteration (Outer Loop)	One iteration (OptiStruct)	Total
Academic example	12 s	6 s	3 h, 31 min
Academic example (10%)	11 s	7 s	2 h, 19 min
Wing shell	23 s	16 s	1 day, 5 h, 36 min
Wing shell (10%)	25 s	18 s	1 day, 7 h, 24 min
Hardware: Laptop, Intel Core i7-1355U @ 1.70 GHz, 16 GB RAM, Windows 10 (×64)			

4. Conclusions and outlook

This study introduces an innovative automated design and optimization method for the production of aerospace components, focusing on VAT laminate designs tailored for complex double-curved structures. The method successfully integrates automated design generation with optimization algorithms that adjust both fiber orientations and laminate thickness, demonstrating its ability to maximize material efficiency and structural integrity while ensuring manufacturability and quality compliance.

The results of this study demonstrate that VAT laminates, when designed through this automated workflow, offer promising weight-saving potential across different structural complexities, from simple academic examples to representative aerospace components. Notably, these benefits were observed even under basic loading conditions, suggesting potentially greater advantages in more complex, real-world scenarios. The consistent production of manufacturable designs ready for AFP production represents a significant step towards the practical implementation of VAT technology in aerospace applications.

Current design rules in aerospace aim to create quasi-isotropic laminates that closely mimic the mechanical properties of replaced metallic components. However, these rules do not fully exploit the potential of composite laminates, particularly VAT designs. To fully leverage the benefits of VAT laminates, a reevaluation and adaptation of these design rules is necessary. This process will require aerospace companies to develop new validation methods to enable the future certification and implementation of VAT laminates in aircraft structures.

By deviating from quasi-isotropic behavior, VAT laminates open up possibilities for aeroelastic tailoring. This approach allows components to deform under load in ways that offer additional advantages. For instance, VAT laminate wings could twist under load to optimize their aerodynamic profile during flight, potentially reducing fuel consumption not only through weight reduction but also through improved aerodynamic performance.

While this study demonstrated weight savings with a single VAT layer design, the incorporation of multiple VAT layer designs could substantially increase weight reduction possibilities, potentially making standard orientation layers obsolete in certain applications. Furthermore, this study utilized full plies exclusively. Additional optimization of ply contours would likely contribute to further weight reductions, although it is worth noting that such contour optimizations would also benefit classical laminates by reducing their weight through the avoidance of full plies.

It is important to acknowledge that this study did not address shuffle optimization, a process that rearranges the stacking sequence of plies to improve laminate performance, which can be easily appended to the current workflow to produce a finalized laminate design. This additional step would allow for the implementation of further design rules and potentially enhance the overall performance of the laminate.

Looking forward, further investigation into the performance of VAT laminates under more complex, multi-load case scenarios will be crucial for fully understanding their benefits in real-world aerospace applications. The continued refinement of the automated design workflow, coupled with experimental investigation of manufacturing constraints is crucial for producing defect-free VAT laminates. This includes factors such as the minimum steering radius, which depends not only on the AFP machine capabilities but also on process parameters like pressure and temperature. Further research into these manufacturing aspects, coupled with experimental validation of the optimized designs, will be essential steps in ensuring the real-world applicability and reliability of this method.

Moreover, the database generated through this automated design process offers significant potential beyond its immediate application. It can serve as a valuable resource for training neural networks, particularly for large-scale tools dealing with complex geometries, curvatures, or load cases. This approach could dramatically enhance the efficiency and applicability of VAT design optimization for more intricate aerospace components, potentially leading to even greater weight savings and performance improvements.

Furthermore, the optimization toolbox developed in this study offers significant potential for future enhancements. It can be extended to analyze the robustness of designs with respect to manufacturing uncertainties. This capability would allow engineers to select designs that, while potentially offering slightly less weight reduction, are more resilient to stochastic manufacturing inaccuracies.

In conclusion, this study represents a significant advancement in the field of composite design for aerospace applications. By bridging the gap between innovative VAT concepts and practical manufacturing constraints, it paves the way for the next generation of lightweight, high-performance aerospace structures. The continued development and refinement of such automated design and optimization methods will be crucial for fully leveraging the benefits of advanced composite technologies in real-world applications.

CRediT authorship contribution statement

Pezhman Pourabdollah: Writing – original draft, Visualization, Validation, Software, Project administration, Methodology, Investigation, Formal analysis, Data curation, Conceptualization. **Lennart Finger:** Writing – review & editing, Validation, Conceptualization. **Rachid Alhourani:** Writing – review & editing, Validation, Software. **Tim Frerich:** Writing – review & editing, Conceptualization. **Raphael Höfer:** Conceptualization, Writing – review & editing. **Felix Gehlhoff:** Writing – review & editing, Supervision, Conceptualization. **Benedikt Kriegesmann:** Writing – review & editing, Supervision, Conceptualization.

Declaration of competing interest

The authors declare the following financial interests/personal relationships which may be considered as potential competing interests: Lennart Finger reports a relationship with Airbus Operations GmbH that includes: employment. Tim Frerich reports a relationship with Airbus Operations GmbH that includes: employment. If there are other authors, they declare that they have no known competing financial interests or personal relationships that could have appeared to influence the work reported in this paper.

Acknowledgments

This research paper, part of the project LaiLa – Laboratory for Intelligent Lightweight Production, is funded by dtec.bw – Digitalization and Technology Research Center of the Bundeswehr which we gratefully acknowledge. dtec.bw is funded by the European Union – NextGenerationEU.

Data availability

Data will be made available on request.

References

[1] Chawla KK. Composite materials: Science and engineering. Cham: Springer International Publishing; 2019, http://dx.doi.org/10.1007/978-3-030-28983-6.
[2] Daniel IM, Ishai O. Engineering mechanics of composite materials. 2nd ed.. New York, NY: Oxford Univ. Press; 2006.
[3] Lukaszewicz DHJA, Ward C, Potter KD. The engineering aspects of automated prepreg layup: History, present and future. Compos Part B: Eng 2012;43(3):997–1009. http://dx.doi.org/10.1016/j.compositesb.2011.12.003.
[4] Roeseler WG, Sarh B, Kismarton MU. Composite structures: The first 100 years. In: Composite structures.
[5] Lukaszewicz DHJA. Optimisation of high-speed automated layup of thermoset carbon-fibre preimpregnates (Ph.D. thesis), Bristol: University of Bristol; 2011.
[6] Lukaszewicz D-J, Weaver PM, Potter K. An automated ply collation system for material and process development. In: SAMPE seico. Paris; 2010.
[7] Kozaczuk K. Automated fiber placement systems overview. Pr Inst Lotnictwa 2016;(4 (245)):52–9. http://dx.doi.org/10.5604/05096669.1226355.
[8] Brasington A, Sacco C, Halbritter J, Wehbe R, Harik R. Automated fiber placement: A review of history, current technologies, and future paths forward. Compos Part C: Open Access 2021;6. http://dx.doi.org/10.1016/j.jcomc.2021.100182.
[9] Kim B, Weaver P, Potter K. Manufacturing characteristics of the continuous tow shearing method for manufacturing of variable angle tow composites. Compos Part A: Appl Sci Manuf 2014;61:141–51. http://dx.doi.org/10.1016/j.compositesa.2014.02.019.
[10] Groh RM, Weaver P. Mass optimisation of variable angle tow, variable thickness panels with static failure and buckling constraints. In: 56th AIAA/ASCE/AHS/ASC structures, structural dynamics, and materials conference. Kissimmee, Florida: American Institute of Aeronautics and Astronautics; 2015, http://dx.doi.org/10.2514/6.2015-0452.
[11] Xu Y, Zhu J, Wu Z, Cao Y, Zhao Y, Zhang W. A review on the design of laminated composite structures: Constant and variable stiffness design and topology optimization. Adv Compos Hybrid Mater 2018;1(3):460–77. http://dx.doi.org/10.1007/s42114-018-0032-7.
[12] Ghiasi H, Pasini D, Lessard L. Optimum stacking sequence design of composite materials Part I: Constant stiffness design. Compos Struct 2009;90(1):1–11. http://dx.doi.org/10.1016/j.compstruct.2009.01.006.
[13] Ghiasi H, Fayazbakhsh K, Pasini D, Lessard L. Optimum stacking sequence design of composite materials Part II: Variable stiffness design. Compos Struct 2010;93(1):1–13. http://dx.doi.org/10.1016/j.compstruct.2010.06.001.
[14] Technomic Publishing Company, editor. The composite materials handbook: MIL 17. Lancaster: Technomic Publ; 1999.
[15] Niu MC-Y. Composite airframe structures: Practical design information and data. Second edition, fifth published ed.. Hong Kong: Conmilit Press LTD; 2008.
[16] Fayazbakhsh K, Arian Nik M, Pasini D, Lessard L. Defect layer method to capture effect of gaps and overlaps in variable stiffness laminates made by Automated Fiber Placement. Compos Struct 2013;97:245–51. http://dx.doi.org/10.1016/j.compstruct.2012.10.031.
[17] Zhao W, Kapania R. Buckling analysis and optimization of stiffened variable angle tow laminates with a cutout considering manufacturing constraints. J Compos Sci 2022;6(3). http://dx.doi.org/10.3390/jcs6030080.
[18] Kazemi M, Verchery G. Design of composite laminated plates for maximum buckling load with stiffness and elastic modulus constraints. Compos Struct 2016;148:27–38. http://dx.doi.org/10.1016/j.compstruct.2016.03.051.
[19] Autio M. Optimization of coupled thermal-structural problems of laminated plates with lamination parameters. Struct Multidiscip Optim 2001;21(1):40–51. http://dx.doi.org/10.1007/s001580050166.
[20] Nikbakt S, Kamarian S, Shakeri M. A review on optimization of composite structures Part I: Laminated composites. Compos Struct 2018;195. http://dx.doi.org/10.1016/j.compstruct.2018.03.063.
[21] Heinecke F, Willberg C. Manufacturing-induced imperfections in composite parts manufactured via automated fiber placement. J Compos Sci 2019;3(2). http://dx.doi.org/10.3390/jcs3020056.
[22] Brooks TR, Martins JR. On manufacturing constraints for tow-steered composite design optimization. Compos Struct 2018;204:548–59. http://dx.doi.org/10.1016/j.compstruct.2018.07.100.
[23] Sawicki A, Minguett P. The effect of intraply overlaps and gaps upon the compression strength of composite laminates. In: 39th AIAA/ASME/ASCE/AHS/ASC structures, structural dynamics, and materials conference and exhibit. American Institute of Aeronautics and Astronautics, http://dx.doi.org/10.2514/6.1998-1786.
[24] Croft K, Lessard L, Pasini D, Hojjati M, Chen J, Yousefpour A. Experimental study of the effect of automated fiber placement induced defects on performance of composite laminates. Composites Part A: Applied Science and Manufacturing 2011;42(5):484–91. http://dx.doi.org/10.1016/j.compositesa.2011.01.007.
[25] Dutta S, Zhao W. Buckling of variable angle tow steered laminates considering gap/overlap defects identified using innovative image processing. Compos Struct 2025;368:119221. http://dx.doi.org/10.1016/j.compstruct.2025.119221.
[26] Füssel L, Cender T, Austermann V, Gillespie J, Heider D. Tow Steering of stretchable TUFF thermoplastic tape with laser tape placement. In: Int SAMPE tech conf. Vol. 2022-May, Soc. for the Advancement of Material and Process Engineering; 2022.
[27] Jeliazkov M, Abadi P, Lopes C, Abdalla M, Peeters D. Buckling and first-ply failure optimization of stiffened variable angle tow panels. 2015.
[28] Hyer MW, Lee HH. The use of curvilinear fiber format to improve buckling resistance of composite plates with central circular holes. Compos Struct 1991;18(3):239–61. http://dx.doi.org/10.1016/0263-8223(91)90035-W.
[29] Aoki Y, Sasaki K, Sugimoto S, Nakamura T. Design and evaluation of load path tailored composite panels. In: Proceedings of the american society for composites â€" Thirty-fifth technical conference. 2020, http://dx.doi.org/10.12783/asc35/34867.
[30] Brandmaier HE. Optimum filament orientation criteria. J Compos Mater 1970;4(3):422–5. http://dx.doi.org/10.1177/002199837000400314.
[31] Cooper AAG. Trajectory fiber reinforcement of composite structures (Ph.D. thesis), St. Louis: Washington Univ.; 1972.
[32] Drach B, Kuksenko D, Sevostianov I. Effect of a curved fiber on the overall material stiffness. Int J Solids Struct 2016;100–101:211–22. http://dx.doi.org/10.1016/j.ijsolstr.2016.08.018.
[33] Rashed A, Demir E. Design of variable stiffness composites for maximum fundamental frequency considering manufacturing constraints of tow steering. Compos Struct 2022;284. http://dx.doi.org/10.1016/j.compstruct.2021.115151.
[34] Khajah T, Natarajan S. Layup optimization of tow-steered composite laminates for maximum fundamental frequency and flutter speed using differential evolution. Compos Struct 2023;310:116748. http://dx.doi.org/10.1016/j.compstruct.2023.116748.
[35] Zhang K, Liu D, Wang Q, Hao P, Duan Y, Tang H, Wang B. Multi-level intelligent design of variable angle tow laminates via image-driven method. Compos Struct 2023;303. http://dx.doi.org/10.1016/j.compstruct.2022.116354.
[36] Zhou X-Y, Ruan X, Gosling PD. Thermal buckling optimization of variable angle tow fibre composite plates with gap/overlap free design. Compos Struct 2019;223:110932. http://dx.doi.org/10.1016/j.compstruct.2019.110932.
[37] Hyer MW, Charette RF. Innovative design of composite structures: Use of curvilinear fiber format to improve structural efficiency. Technical Report TR-87-5, 1987.
[38] Khani A, IJsselmuiden ST, Abdalla MM, Gürdal Z. Design of variable stiffness panels for maximum strength using lamination parameters. Compos Part B: Eng 2011;42(3):546–52. http://dx.doi.org/10.1016/j.compositesb.2010.11.005.
[39] Thomas M, Weaver P, Hallett S. Variable stiffness composite laminates for doubly curved plates using lamination parameters. In: ICCM int. conf. compos. mater.. Vol. 2017-August, International Committee on Composite Materials; 2017.
[40] Khani A. Optimum design of steered fibre composite cylinders with arbitrary cross-sections (Ph.D. thesis), [object Object]; 2013.
[41] Montemurro M, Catapano A. A new paradigm for the optimum design of variable angle tow laminates. 2016.
[42] Setoodeh S, Abdalla MM, Gürdal Z. Design of variable–stiffness laminates using lamination parameters. Compos Part B: Eng 2006;37(4):301–9. http://dx.doi.org/10.1016/j.compositesb.2005.12.001.
[43] Montemurro M, Catapano A. On the effective integration of manufacturability constraints within the multi-scale methodology for designing variable angle-tow laminates. Compos Struct 2017;161:145–59. http://dx.doi.org/10.1016/j.compstruct.2016.11.018.
[44] Noevere AT, Collier C. Development of a design for manufacturing tool for automated fiber placement structures. In: AIAA scitech 2020 forum. Reston, Virginia: American Institute of Aeronautics and Astronautics; 2020, p. 1–11. http://dx.doi.org/10.2514/6.2020-1477.
[45] Qu W, He R, Wang Q, Cheng L, Yang D, Gao J, Wang H, Yang Q, Ke Y. Algorithms for constructing initial and offset path of automated fiber placement for complex double-curved surfaces. Appl Compos Mater 2021;28(3):855–75. http://dx.doi.org/10.1007/s10443-021-09901-2.
[46] Arsenyeva A, Duddeck F, Thompson HM. An iso-contour method for automated fiber placement optimization of composite structures. Compos Struct 2024;327:117628. http://dx.doi.org/10.1016/j.compstruct.2023.117628.

[47] Nocedal J, Wright SJ. Numerical optimization. Springer series in operation research and financial engineering, 2nd ed.. New York, NY: Springer; 2006.
[48] Rousseau G, Wehbe R, Halbritter J, Harik R. Automated fiber placement path planning: A state-of-the-art review. Comput-Aided Des Appl 2018;16(2):172–203. http://dx.doi.org/10.14733/cadaps.2019.172-203.
[49] Maekawa T. An overview of offset curves and surfaces. Comput-Aided Des 1999;31(3):165–73. http://dx.doi.org/10.1016/S0010-4485(99)00013-5.
[50] Pekerman D, Elber G, Kim M-S. Self-intersection detection and elimination in freeform curves and surfaces. Comput-Aided Des 2008;40(2):150–9. http://dx.doi.org/10.1016/j.cad.2007.10.004.
[51] Seong J-K, Elber G, Kim M-S. Trimming local and global self-intersections in offset curves/surfaces using distance maps. Comput-Aided Des 2006;38(3):183–93. http://dx.doi.org/10.1016/j.cad.2005.08.002.
[52] Tanaka H, Mori Y, Kumekawa N, Matsuzaki R. Optimization of fiber orientation and layer thickness in thin carbon fiber-reinforced plastic curved structures. Compos Part C: Open Access 2023;12:100381. http://dx.doi.org/10.1016/j.jcomc.2023.100381.
[53] Zenker T, Bruckner F, Drechsler K. Effects of defects on laminate quality and mechanical performance in thermoplastic Automated Fiber Placement-based process chains. Adv Manuf: Polym Compos Sci 2019;5(4):184–205. http://dx.doi.org/10.1080/20550340.2019.1703334.
[54] Wiehn MP, Hale RD. Low cost robotic fabrication methods for tow placement. In: SAMPE 2002 - Long Beach CA. 2002.
[55] Moon RS, Johnson CC, Hale RD. Nondestrcutive evaluation and mechanical testing of steered fiber composites. In: SAMPE 2002 - Long Beach CA. 2002.
[56] Blom AW, Lopes CS, Kromwijk PJ, Gurdal Z, Camanho P. A theoretical model to study the influence of tow-drop areas on the stiffness and strength of variable-stiffness laminates. J Compos Mater 2009;43(5):403–25. http://dx.doi.org/10.1177/0021998308097675.
[57] Costa A, Nannicini G. RBFOpt: An open-source library for black-box optimization with costly function evaluations – Optimization Online. 2014.
[58] Gutmann H-M. A radial basis function method for global optimization. J Global Optim 2001;19(3):201–27. http://dx.doi.org/10.1023/A:1011255519438.
[59] Regis RG, Shoemaker CA. A stochastic radial basis function method for the global optimization of expensive functions. INFORMS J Comput 2007;19(4):497–509. http://dx.doi.org/10.1287/ijoc.1060.0182.